

# Synthesis and characterisation of *A*-site deficient ordered perovskites

Dashnor Beqiri

A thesis presented for the degree of  
Master of Science by Research



Supervisor: Dr Emma E. McCabe

School of Physical Sciences

University of Kent

September 2019

# Contents

<b>1</b>	<b>Introduction</b>	<b>7</b>
1.1	Perovskites . . . . .	7
1.2	Magnetism . . . . .	8
1.3	Ferroelectricity . . . . .	8
1.3.1	Proper Ferroelectricity . . . . .	9
1.3.2	Hybrid Improper Ferroelectricity . . . . .	9
1.4	Layered perovskite-related Structures . . . . .	9
1.4.1	Aurivillius phases . . . . .	10
1.4.2	Ruddlesden-Popper phases . . . . .	10
1.4.3	Dion-Jacobson phases . . . . .	11
1.5	A-site Deficient Perovskites . . . . .	11
1.5.1	A-site deficient niobates ( $Ln_{0.33}NbO_3$ ) . . . . .	12
1.5.2	A-site deficient tantalates ( $Ln_{0.33}TaO_3$ ) . . . . .	13
1.5.3	A-site deficient double perovskites . . . . .	14
1.6	Aims . . . . .	16
<b>2</b>	<b>Experimental and Analytical methodology</b>	<b>17</b>
2.1	Experimental . . . . .	17
2.1.1	Solid State Synthesis . . . . .	17
2.2	Analytical Methods . . . . .	17
2.2.1	Powder X-Ray Diffraction (PXRD) . . . . .	17
2.2.2	Neutron Powder Diffraction (NPD) . . . . .	19
2.2.3	Rietveld Refinements . . . . .	19
2.2.4	Magnetic Susceptibility Measurements (SQUID) . . . . .	19
2.2.5	Density Functional theory (DFT) . . . . .	20
2.2.6	SEM/TEM measurements . . . . .	20
<b>3</b>	<b>Tuning the octahedral tilts in the A-site deficient perovskite <math>Nd_{0.33}NbO_3</math></b>	

<b>through intercalation with Li<sup>+</sup> ions</b>	<b>22</b>
3.1 Introduction . . . . .	22
3.2 Experimental . . . . .	23
3.2.1 Synthesis of Nd <sub>0.33</sub> NbO <sub>3</sub> . . . . .	23
3.2.2 Reductive Intercalation to form Li <sub>x</sub> Nd <sub>0.33</sub> NbO <sub>3</sub> . . . . .	23
3.2.3 Iodometric Titrations . . . . .	23
3.3 Complementary Techniques . . . . .	23
3.3.1 SQUID Magnetometry . . . . .	23
3.3.2 Density Functional Theory . . . . .	23
3.3.3 Electron Diffraction (ED) . . . . .	24
3.4 Results and Discussion . . . . .	24
3.4.1 Synthesis and initial characterisation of Nd <sub>0.33</sub> NbO <sub>3</sub> and Li <sub>x</sub> Nd <sub>0.33</sub> NbO <sub>3</sub>	24
3.4.2 Characterisation of Nd <sub>0.33</sub> NbO <sub>3</sub> by NPD . . . . .	25
3.4.3 Characterisation of Li <sub>x</sub> Nd <sub>0.33</sub> NbO <sub>3</sub> by NPD . . . . .	27
3.4.4 Electron Diffraction of Li <sub>x</sub> Nd <sub>0.33</sub> NbO <sub>3</sub> . . . . .	28
3.4.5 Magnetic Susceptibility measurements . . . . .	29
3.4.6 Density Functional Theory . . . . .	30
3.5 Conclusions and Future Work . . . . .	30
3.5.1 Future Work . . . . .	31
<b>4 Synthesis and characterisation of La<sub>4</sub>Mg<sub>3</sub>W<sub>3</sub>O<sub>18</sub> and La<sub>(4-x)</sub>Nd<sub>x</sub>Mg<sub>3</sub>W<sub>3</sub>O<sub>18</sub></b>	
<b>(0 ≤ x ≤ 2)</b>	<b>32</b>
4.1 Introduction . . . . .	32
4.2 Synthesis of La <sub>4</sub> Mg <sub>3</sub> W <sub>3</sub> O <sub>18</sub> and La <sub>(4-x)</sub> Nd <sub>x</sub> Mg <sub>3</sub> W <sub>3</sub> O <sub>18</sub> (0 ≤ x ≤ 2) . . . . .	33
4.2.1 SEM/EDX analysis . . . . .	34
4.3 Results and Discussion . . . . .	34
4.3.1 La <sub>4</sub> Mg <sub>3</sub> W <sub>3</sub> O <sub>18</sub> . . . . .	34
4.3.2 La <sub>4-x</sub> Nd <sub>x</sub> Mg <sub>3</sub> W <sub>3</sub> O <sub>18</sub> . . . . .	35
4.4 Conclusions and Future work . . . . .	38
4.4.1 Future Work . . . . .	39
<b>5 B-site doping of La<sub>4</sub>Mg<sub>3</sub>W<sub>3</sub>O<sub>18</sub> with Cu/Zn and double B-site substitution</b>	
<b>with Fe/Mn and Ta</b>	<b>40</b>
5.1 Introduction . . . . .	40
5.2 Experimental . . . . .	40
5.2.1 Cu/Zn-doped La <sub>4</sub> Mg <sub>3</sub> W <sub>3</sub> O <sub>18</sub> . . . . .	40
5.2.2 Double substituted La <sub>4</sub> Mg <sub>3</sub> W <sub>3</sub> O <sub>18</sub> . . . . .	41

5.2.3	SEM/EDX analysis . . . . .	41
5.3	Results and Discussion . . . . .	41
5.3.1	Cu-doped $\text{La}_4\text{Mg}_3\text{W}_3\text{O}_{18}$ . . . . .	41
5.3.2	Zn-doped $\text{La}_4\text{Mg}_3\text{W}_3\text{O}_{18}$ . . . . .	44
5.3.3	Fe/Ta doped $\text{La}_4\text{Mg}_3\text{W}_3\text{O}_{18}$ . . . . .	45
5.3.4	Mn/Ta doped $\text{La}_4\text{Mg}_3\text{W}_3\text{O}_{18}$ . . . . .	48
5.4	Conclusions and Future Work . . . . .	48
5.4.1	Future Work . . . . .	49
<b>6</b>	<b>Conclusions and future work</b>	<b>50</b>
6.1	$\text{Li}^+$ insertion into the <i>A</i> -site deficient $\text{Nd}_{0.33}\text{NbO}_3$ . . . . .	50
6.2	<i>A</i> -site doping of the <i>A</i> -site deficient double perovskite $\text{La}_4\text{Mg}_3\text{W}_3\text{O}_{18}$ . . . . .	50
6.3	<i>B</i> -site doping of the <i>A</i> -site deficient double perovskite $\text{La}_4\text{Mg}_3\text{W}_3\text{O}_{18}$ . . . . .	51
6.4	Future work . . . . .	51

# Acknowledgements

Thank you to my Mother and Father, for all of their support throughout this year, and all of the years throughout my degree. Without it, I wouldn't have been able to even get to where I am today. I'm thankful for all the phone calls telling me to keep going, without which, I don't know how I would have done.

Thank you to my partner, Sophie, for all of the mental support and motivation I needed throughout of the year to keep going, especially when things got tough at certain points and I wanted to give up.

To the fantastic Solid-State group for their insight on issues I was having when I had none. Particular mention to Richard and Kevin who had to listen to me ramble on about random parts of my research when they had work to do, as well as helping me with some of the more difficult concepts.

To all of my friends, who made me remember I was human, and had a soul, so pulled me out of work to have lunch, or play games when I got stressed. To all of my DnD friends, thank you for dragging me out of this complicated world into an even more complicated one, and for understanding when things got stressful.

To all the streamers online who got me through this thesis just by being in the background whilst I worked.

Finally to Emma and Vanessa. Vanessa, thank you for making me realise that things take time, and that nothing comes out perfect the first time. Also making me realise that I do know things.

Emma, thank you for giving me a chance to prove what I can do. When I came to work with you in second year, I knew nothing, now I know a lot about this, and it's all because of you. I'm truly grateful for your patience with me and my enthusiasm, particularly when you were so stressed. Thank you for being the reason I got into solid-state chemistry.

# Declaration

I declare that the thesis has been composed by myself and that the work has not be submitted for any other degree or professional qualification. I confirm that the work submitted is my own, except where work which has formed part of jointly-authored publications has been included. My contribution and those of the other authors to this work have been explicitly indicated below. I confirm that appropriate credit has been given within this thesis where reference has been made to the work of others.

The work presented in Chapter 3 was previously published in *Chemical Communications* as 'Tuning octahedral tilts and the polar nature of *A*-site deficient perovskites' by Dashnor Beqiri (student), Vanessa Cascos, Jennie Roberts-Watts, Ewan R. Clark, Eric Bousquet, Nicholas C. Bristowe and Emma E. McCabe (supervisor).

# Abstract

Recent solid-state research has focused on 2D layered perovskite structures, due to their wide range of properties, such as photocatalytic, magnetic and ferroelectric properties. There are many kinds of layered perovskite-related structures, including Ruddlesden-Popper, Aurivillius and Dion-Jacobson compounds. All three are structurally related but with different layers between perovskite blocks. Recent research, however has been drawn to these two-thirds occupied *A*-site deficient perovskites, due to the  $BO_6$  octahedra maintaining 3D connectivity but having a 2D nature through the ordering of the *A*-site cations.<sup>1</sup>

Ferroelectricity is the spontaneous reversible polarisation of a material upon the application of an electric field. Some layered structures have the potential to display hybrid-improper ferroelectricity; hence they are a topic of research for many solid-state research groups around the world. Hybrid-improper ferroelectricity comes from the coupling of two non-polar distortions (such as octahedral rotations) to break inversion symmetry and induce a ferroelectric effect.

Both  $Nd_{0.33}NbO_3$  and  $Li_xNd_{0.33}NbO_3$  were successfully synthesised and analysed using various techniques, such as PXRD, NPD, SEM, SQUID and DFT. It was seen, from analysis, that the structure undergoes a phase transition to  $P4/mmm$  symmetry upon  $Li^+$  insertion. Solid solutions of  $La_4Mg_3W_3O_{18}$  doped with various elements, such as *A*-site doping with Nd, *B*-site doping with Cu and Zn, as well as double *B*-site substitution with Fe/Ta and analysed using various techniques, such as PXRD, SQUID and SEM. It was found that small amounts of dopant could be put into a structure, however, some of the solid solutions were extremely limited.

# Chapter 1

## Introduction

### 1.1 Perovskites

The perovskite structure is named after the mineral calcium titanate ( $\text{CaTiO}_3$ , Figure 1.1). It was first discovered in the Ural Mountains in Russia in 1839 by Gustav Rose and named after Count Perovsky. The general formula of these perovskite-like structures is  $ABX_3$ , where  $A$  and  $B$  are cationic, and  $X$  is anionic.

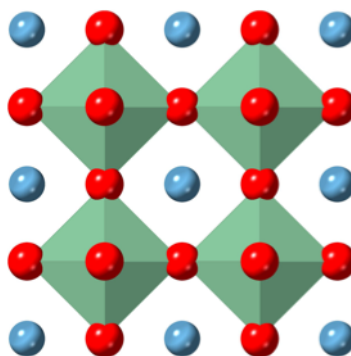


Figure 1.1: *An illustration of the ideal  $ABX_3$  perovskite structure showing  $A$  and  $X$  ions in blue and red, respectively, and  $BX_6$  octahedra in green.*<sup>2</sup>

The  $A$ -site cation is usually the larger cation in the structure, typically a larger group one or two metal cation, or a larger lanthanide ion. The  $B$ -site cations are smaller cations, often transition metals. The  $X$  anions are often oxide ions, however there are kinds of perovskite-related structures, such as MAPI (Methylammonium Lead Iodide) which have the halide ions on the anion sites. There are now many different kinds of perovskite structures, such as MOFs (Metal—Organic Frameworks), and perovskites exhibit a wide variety of properties, such as ferroelectricity<sup>3</sup> and magnetism.<sup>4</sup>

## 1.2 Magnetism

Magnetism arises from the behaviour of unpaired electrons, and the response to an applied magnetic field can be described as diamagnetic, paramagnetic, ferromagnetic, antiferromagnetic or ferrimagnetic. Ferromagnetic behaviour is a property whereby the moments of unpaired electrons are aligned parallel, unlike antiferromagnetic behaviour, where the magnetic moments are aligned antiparallel to each other; in a ferrimagnet, moments are again antiparallel but unequal in size, resulting in a net magnetic moment. Paramagnetic behaviour, on the other hand, is where the magnetic moments are randomly oriented. Diamagnetic behaviour is where the unpaired electron spins in a structure are repelled by a magnetic field. Magnetism in extended structures can also be tuned; for example, in  $\text{La}_{1-x}\text{Sr}_x\text{MnO}_3$ , the structure is tuned between ferromagnetic and antiferromagnetic depending on the La:Sr ratio.<sup>5</sup>

## 1.3 Ferroelectricity

Ferroelectricity is when there is a spontaneous reversible polarisation of a material upon the application of an electric field (as seen in Figure 1.2). This spontaneous polarisation comes from the electric dipoles within the structure ordering in the same direction. This property comes from the polar displacement of cations relative to anions within a non-centrosymmetric structure, such as the displacement of Ti in  $\text{PbTiO}_3$ , meaning that the magnitude of the polarisation is dependant on the electron configuration of the ion being displaced.

This is analogous to ferromagnetism, as it involves alignment of electric dipoles within a structure due to an applied electric field. Due to their spontaneous polarisation, there is a wide range of potential application for materials that show this property, such as non-volatile memories and mass data storage.<sup>6</sup>

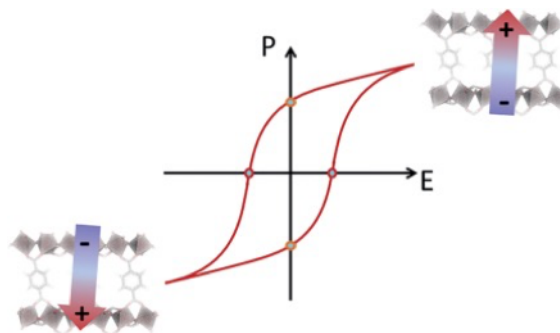


Figure 1.2: A diagram showing the dependence of polarisation ( $P$ ) on an applied electric field ( $E$ )<sup>7</sup>

### 1.3.1 Proper Ferroelectricity

Proper ferroelectricity usually relies on the electronic structure of one or more of the cations within the structure, as the ferroelectricity in the structure is driven by the displacement of one of these ions. An example of proper ferroelectricity is that found in one of the polar phases of  $\text{BaTiO}_3$ , whose origin was found by Megaw in 1952.<sup>8</sup> Above  $130^\circ\text{C}$ ,  $\text{BaTiO}_3$  adopts a non-polar cubic structure, but on cooling, undergoes phase transitions to polar tetragonal and then polar rhombohedral phases.<sup>9</sup>

An important feature of proper ferroelectricity is that the permittivity of the compound is dependent on temperature.

### 1.3.2 Hybrid Improper Ferroelectricity

In contrast, hybrid improper ferroelectricity arises from the coupling of two non-polar distortions that break the inversion symmetry and induce a ferroelectric effect in the structure. The coupling of these non-polar distortions, such as the tilting and the rotation of  $\text{BO}_6$  octahedra,<sup>10</sup> break the inversion centre of a structure and stabilises polar displacements. The reduction in symmetry induces a polar change in the structure.<sup>11</sup>

The balance between octahedral tilting and cation displacements depends on the ionic size and the configurations of the cations, meaning that the balance between proper and hybrid improper ferroelectricity can be tuned. There are many potential technological applications for improper ferroelectrics.<sup>12</sup> An example of this, is the Ruddlesden-Popper phase  $\text{Ca}_3\text{Mn}_2\text{O}_7$  characterised by Lobanov in 2004.<sup>4</sup> The  $\text{MnO}_6$  octahedra are significantly tilted so as to satisfy the coordination environment of the  $\text{Ca}^{2+}$ , such that the inversion symmetry is broken, giving rise to ferroelectricity through the hybrid improper mechanism. Hybrid improper ferroelectricity differs from proper ferroelectricity in that the permittivity is independent of temperature.

## 1.4 Layered perovskite-related Structures

A focus of recent research has been 2D layered perovskite-related structures due to the wide variety of potential applications for these compounds, such as photocatalytic properties.<sup>13</sup> Other properties have also been investigated, such as magnetic and dielectric properties, in particular their potential for ferroelectric properties through the hybrid improper mechanism.<sup>3</sup> Layered perovskite-related structures include the Ruddlesden-Popper, Aurivillius and Dion-Jacobson family of compounds (see Figure 1.3). All three are structurally related but differ with respect to the layers between the perovskite blocks. These structures have a wide

variety of potential applications, such the potential for hybrid improper ferroelectricity in these structures due to their layered nature and their compositional and structural flexibility.

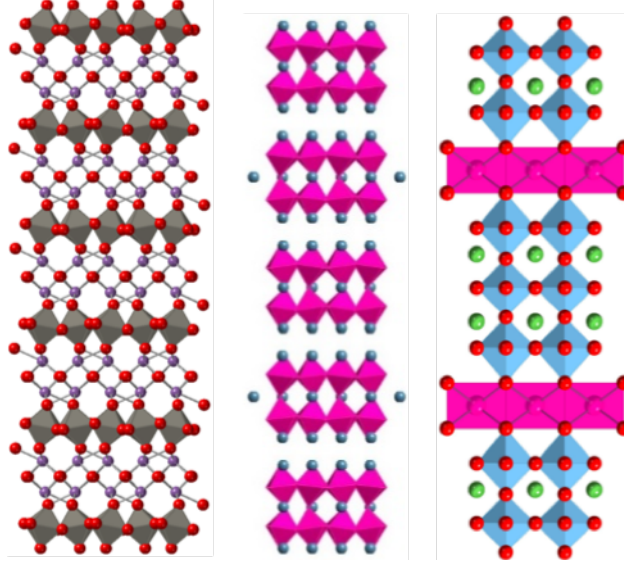


Figure 1.3: A diagram showing the crystal structure of the Aurivillius phase  $\text{Bi}_2\text{WO}_6$  as characterised by Rae et al,<sup>14</sup> the Ruddlesden-Popper phase  $\text{Ca}_3\text{Mn}_2\text{O}_7$  characterised by Lobanov et al,<sup>4</sup> and the Dion-Jacobson phase  $\text{RbLa}_2\text{Ti}_2\text{NbO}_{10}$  characterised by Hong et al<sup>15</sup>

#### 1.4.1 Aurivillius phases

Aurivillius structures have the general formula  $\text{Bi}_2\text{A}_{n-1}\text{B}_n\text{O}_{3n+3}$  and were first discovered in 1949 by Bengt Aurivillius.<sup>16</sup> Their structures are composed of perovskite blocks stacked along the [001], separated by fluorite  $[\text{Bi}_2\text{O}_2]^{2+}$  layers (see Figure 1.3, left).

The fluorite-like layer is preferentially occupied by non-spherical, inert pair ions, such as  $\text{Bi}^{3+}$  and  $\text{Pb}^{3+}$ , whilst the *A*-site of the perovskite block contains a higher concentration of spherical ions. The range of atoms that can sit in the *B*-site is much less than that of the perovskite structure and the Ruddlesden-Popper family.

#### 1.4.2 Ruddlesden-Popper phases

This range of compounds was first discovered in 1958, when Ruddlesden and Popper characterised  $\text{Sr}_3\text{Ti}_2\text{O}_7$  and  $\text{Sr}_2\text{TiO}_4$ .<sup>17</sup> These materials have the general formula  $\text{A}_{n+1}\text{B}_n\text{O}_{3n+1}$ . In between each of the perovskite blocks in the structure, is an *AO* rock salt like layer. As with the Aurivillius phase, the *A*-site accommodates larger cations, whereas the *B*-sites are occupied by smaller cations, such as iron<sup>18</sup> (see Figure 1.3, centre). Recent theoretical and experimental studies have shown that Ruddlesden-Popper phases, such as  $\text{Ca}_3\text{Mn}_2\text{O}_7$ ,<sup>4</sup> have the potential to be hybrid improper ferroelectrics.<sup>10</sup>

### 1.4.3 Dion-Jacobson phases

This layered structure has the general formula  $A'[A_{n-1}B_nO_{3n+1}]$ . This kind of layered structure was first discovered by Dion in 1981<sup>19</sup> and further researched by Jacobson in 1986.<sup>20</sup> On the 8-coordinate  $A'$ -site, there would usually be an alkali metal, such as potassium, caesium or rubidium, due to their ability to form large coordination environments (see Figure 1.3, right). The metals on the  $A$ -site are usually group 2 metals, like calcium or strontium; or the larger lanthanide cations, like lanthanum or neodymium.

As with the other two phases, the  $B$ -site is where the smaller cations, such as transition metals sit, due to their size and their ability to coordinate in a corner-shared octahedral conformation. As with the other layered structures, Dion-Jacobson phases also have the potential of being hybrid improper ferroelectrics<sup>10</sup> and have a wide variety of applications, more recently photovoltaics,<sup>13</sup> where the phase has an organic molecule in the  $A'$ -site. However, recent work has shown that separating the perovskite blocks along the  $[001]$  direction reduces the correlation length of structural distortions along  $[001]$ <sup>21</sup> which could be detrimental to properties.

## 1.5 $A$ -site Deficient Perovskites

Perovskite materials have also been discovered in which the  $A$ -sites are only partially occupied in an ordered fashion. The  $A$ -site cations in these materials are ordered in layers, with alternating partially occupied and vacant layers within the structure (see Figure 1.4). They have the potential to be hybrid improper ferroelectrics because of their layered nature. However, due to the three-dimensional connectivity of the  $BO_6$  octahedra, the correlation length of polar distortions is likely to be larger than in the Dion-Jacobson phases, improving physical properties. Lanthanide tantalate and niobate compounds are most commonly studied due to their ability to adopt polar structures.<sup>22,23</sup>

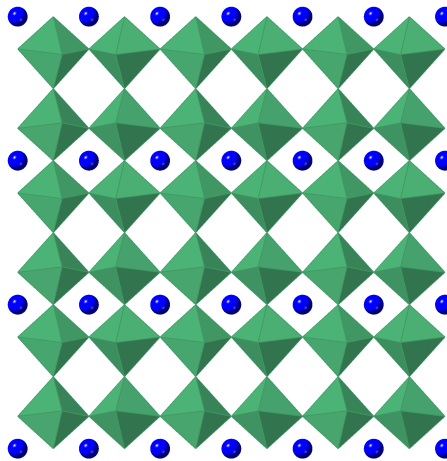


Figure 1.4: A diagram showing the crystallographic presentation of the A-site deficient perovskite  $La_{0.33}NbO_3$ , with the La atoms in blue, and the Nb octahedra in green. Space group:  $Cmmm$ <sup>24</sup>

### 1.5.1 A-site deficient niobates ( $Ln_{0.33}NbO_3$ )

Results have only been published for the larger lanthanide niobate compounds, such as the ones containing lanthanum and neodymium<sup>22,25</sup>. The smaller lanthanide niobates have not been reported. Earlier work on the  $Ln_{0.33}NbO_3$  phases reported structures of several different symmetries, but studies using NPD have suggested that a model of  $Cmmm$  symmetry ( $a^- b^0 c^0$  tilts) best describes their crystal structures (see Table 1.1).

On heating, the  $Ln_{0.33}NbO_3$  structures undergo a phase transition from the  $Cmmm$  structure to the tetragonal  $P4/mmm$  structure as the  $a^- b^0 c^0$  tilt is lost. For example,  $Nd_{0.33}NbO_3$  undergoes a phase transition from  $Cmmm$  to  $P4/mmm$  at 650°C.<sup>22</sup>

### 1.5.2 A-site deficient tantalates ( $Ln_{0.33}TaO_3$ )

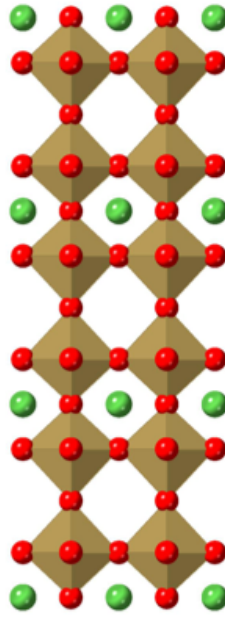


Figure 1.5: A diagram showing the crystallographic presentation of the A-site deficient perovskite  $La_{0.33}TaO_3$ , with the La atoms in blue, the Ta octahedra in brown and the O atoms in red. Space group:  $P4/mmm$ <sup>23</sup>

The symmetries of the tantalate analogues (see figure 1.5) are similar to those of the niobates, but a wider range of  $Ln^{3+}$  analogues have been reported<sup>23</sup>(see Table 1.1). The symmetry of the  $Ln_{0.33}NbO_3$  is lowered with decreasing  $Ln^{3+}$  radius, with polar structures being reported for  $Ln = Ho, Er$ . The magnitude of the tilts of the  $TaO_6$  octahedra increase with decreasing  $Ln^{3+}$ , something which is seen in the niobate analogues<sup>26</sup> and the corresponding titanate analogues.<sup>27</sup>

Table 1.1: Table showing the structural comparison between the *A*-site deficient tantalates and niobates at room temperature

Lanthanide	Tantalate analogue	Niobate analogue
La	$P4/mmm$ <sup>23</sup>	$Cmmm$ <sup>26</sup>
Ce	$Cmmm$ <sup>23</sup>	-
Pr	$Cmmm$ <sup>23</sup>	$Cmmm$ <sup>22</sup>
Nd	$Cmmm$ <sup>23</sup>	$Cmmm$ <sup>28</sup>
Pm	-	-
Sm	$Cmmm$ <sup>23</sup>	-
Eu	$Cmmm$ <sup>23</sup>	-
Gd	$Cmmm$ <sup>23</sup>	-
Tb	$Pbmm(Pnma)$ <sup>23</sup>	-
Dy	$Pbmm(Pnma)$ <sup>23</sup>	-
Ho	$P2_1am(Pmc2_1)$ <sup>23</sup>	-
Er	$P2_1am(Pmc2_1)$ <sup>23</sup>	-
Tm	Incommensurate <sup>23</sup>	-
Yb	-	-
Lu	-	-

### **A-site deficient titanates ( $Ln_{0.67}TiO_3$ )**

There has been some research into *A*-site deficient lanthanide titanates.<sup>27,29</sup> Various analogues have been synthesised and analysed, with further analysis done on lanthanum and neodymium only.<sup>30</sup> The tilting in these compounds again depends on the size of the lanthanide ion: the smaller the ion, the bigger the tilt. In these structures, however, the octahedral tilting is competing with some second order Jahn-Teller effects from the  $TiO_6$  themselves, just as in the Nb and Ta analogues.<sup>30</sup> Intercalations on lanthanum and neodymium analogues have been done, meaning that elements such as lithium and calcium can be put into the vacant sites.<sup>30,31</sup>

### **1.5.3 A-site deficient double perovskites**

Perovskite structures containing two kinds of *B*-site cations (*B* and *B'*), which differ in size and charge, can adopt *B*-site ordered structures, in which the  $BO_6$  and  $B'O_6$  are arranged in a checkerboard, or rock salt fashion (such as  $Ba_2MnWO_6$ ,<sup>32</sup> Figure 1.6). This therefore makes the general formula for these double perovskite structures  $A_2BB'X_6$ .<sup>33</sup> In addition to *B*-site ordering, *A*-site ordering can also occur, more commonly in layers, giving the general

formula  $AA'BB'X_6$ . An example of this is in the double perovskite structure  $\text{NaLaMWO}_6$  (where  $M = \text{Co}, \text{Ni}$ ).<sup>34</sup> In the structure of this double perovskite, the sodium and lanthanum ions are ordered in alternating layers<sup>34</sup>.

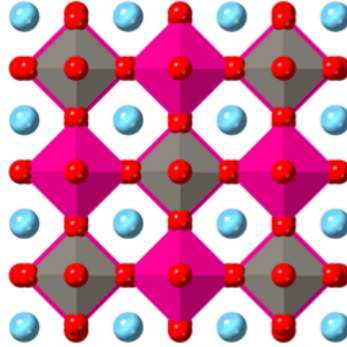


Figure 1.6: A diagram showing the double perovskite structure  $\text{Ba}_2\text{MnWO}_6$  as characterised by Azad et al.<sup>33</sup> The Ba atoms are in blue, the Mn octahedra in pink, and the W octahedra are in grey

In principle,  $A$ -site deficient  $B$ -site ordered perovskites should also exist and two have been reported:  $\text{La}_4\text{Mg}_3\text{W}_3\text{O}_{18}$ <sup>35</sup> and  $\text{La}_{5/3}\text{MgTaO}_6$ .<sup>36</sup> Both have checkerboard ordering of  $B$ -site cations described using the  $R1+$  irrep, (see Figure 1.7).  $\text{La}_4\text{Mg}_3\text{W}_3\text{O}_{18}$  also has a complicated ordering of  $\text{La}^{3+}$  cations and vacancies described using the  $Z4$  irrep. These lower symmetry perovskite structures involving cation-ordering or octahedral rotations can be described in terms of the parent perovskite structure with symmetry-adapted distortion modes (either occupancy or displacive modes, corresponding to, for example, checkerboard ordering, or octahedral rotations) imposed on it. In this work, these modes were explored using the ISODISTORT software<sup>37</sup> and are labelled by their irreducible representations (irreps) relative to the parent  $Pm\bar{3}m$  perovskite structure.

Combined, this  $A$  and  $B$ -site ordering lowers the symmetry of the structure to the  $Ibam$  symmetry (see Figure 1.7).  $\text{La}_4\text{Mg}_3\text{W}_3\text{O}_{18}$  adopts this structure above 700 K, but on cooling, undergoes a phase transition to a monoclinic structure of  $C2/m$  symmetry, which in addition to the  $A$  and  $B$ -site ordering, this transition also allows  $a^-b^0c^0$  tilts, described by the  $R4+$  irrep (see Figure 1.7).

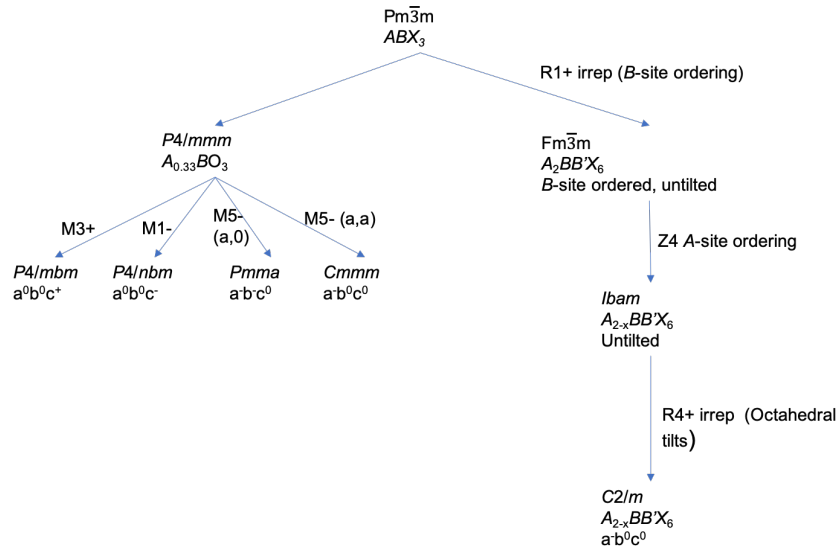


Figure 1.7: A symmetry map showing range of tilt and ordering distortions that a structure can undergo with respect to the  $Pm\bar{3}m$  space group

## 1.6 Aims

Our aims in investigating the  $A$ -site deficient perovskites were to explore their compositional flexibility and whether this could be used to tune structure (e.g. octahedral tilting) and properties (e.g. polar properties, or by introducing magnetic ions). The research described in this thesis had the following aims:

- To investigate whether reductive cation insertion reactions could tune the structure and properties of  $Nd_{0.33}NbO_3$

To investigate the compositional-flexibility through the doping of  $La_4Mg_3W_3O_{18}$  including:

- Investigating whether smaller  $Ln^{3+}$  ions can be introduced to the  $A$ -sites
- Investigating whether  $Zn^{2+}$  or  $Cu^{2+}$  ions can be introduced to the  $Mg^{2+}$   $B$ -sites
- Investigating whether magnetic ions such as  $Fe^{3+}$  or  $Mn^{3+}$  can be introduced to the perovskite  $B$ -sites by a double substitution strategy

## Chapter 2

# Experimental and Analytical methodology

## 2.1 Experimental

### 2.1.1 Solid State Synthesis

This is the most common route used in solid-state chemistry to synthesise polycrystalline samples. It involves taking solid oxide reagents, grinding them in an agate pestle and mortar and heating them at high temperatures in a furnace. There are many issues related to this synthetic route. One of the main issues is that this type of reaction is diffusion limited. In order for the reagents to react this way, high temperatures and long reaction times are required to overcome the diffusion barrier. The main reason that diffusion is so slow in these reactions is that the energy requirement is usually very high.

As a result of the high temperatures required, there is little to no kinetic control over the product formed. This means that the product obtained will almost always be the most thermodynamically stable phase, meaning that the macro, or microstructure desired may not be obtained. Some control may be obtained by quenching the reaction from a high temperature, which allows some access to metastable structures.

## 2.2 Analytical Methods

### 2.2.1 Powder X-Ray Diffraction (PXRD)

X-Ray Powder Diffraction (PXRD) is a powerful tool when it comes to determining phase purity of a product, as well as the size and symmetry of its unit cell. A cathode ray tube (CRT) generates X-Rays through the heating of a filament, which produces high energy

electrons. The electrons are then accelerated through the application of a voltage towards a target and X-rays are generated when an accelerated electron excites an electron from the inner shell of the target metal and cause an electron to relax to the ground state, emitting an X-ray. These X-rays are focused onto the sample and scattered by its crystalline lattice (see Figure 2.1).

The interaction of the incident rays with the sample produces constructive interference (and a diffracted ray) when conditions satisfy Bragg's Law, where Bragg's law is:

$$n\lambda = 2d \sin \theta \quad (2.1)$$

where  $n$  is an integer,  $\lambda$  is equal to the wavelength of the radiation (Cu has a  $K\alpha_1$  wavelength of 1.5406 Å),  $d$  is equal to the spacing in between layers of atoms and  $\theta$  is equal to the angle of the diffracted X-Ray.

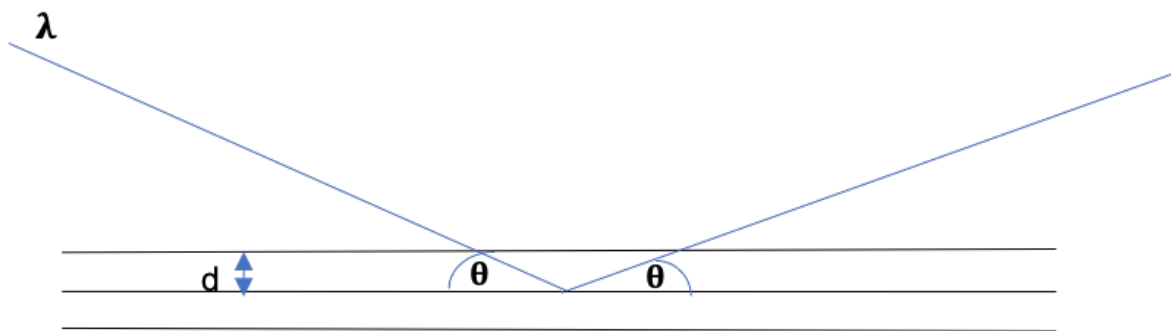


Figure 2.1: A diagram representing Bragg's law

PXRD is a very easy analytical method, due to its availability, as well as the time taken for each pattern to run. X-rays are scattered by electron density in the crystalline sample, meaning that PXRD also works well when the elements being analysed are electron dense, such Nb, or Bi, or any of the  $L_n$  elements. However, when there are light elements in a structure (such as lithium and oxygen), it becomes more difficult to determine their atomic positions within the structure due to the lack of sensitivity.

Room temperature powder X-Ray diffraction (PXRD) patterns were collected using a Rigaku miniflex 6000 with Cu  $K\alpha$  radiation (40 kV, 15 mA) and a D/tEX Ultra detector. Low temperature PXRD patterns were obtained using a PANalytical Empyrean diffractometer (with a Ge monochromator, an X'Celerator detector and an Oxford Cryosystems Phenix Cryostat).

### 2.2.2 Neutron Powder Diffraction (NPD)

NPD is complementary to PXRD in that neutrons are scattered by nuclei in a crystalline sample, often giving greater sensitivity to lighter elements, such as oxygen. This means that we are able to learn more about the role of oxygen in phase transitions, as it allows us to be able to see tilting and other symmetry breaking operations. Neutrons can also be scattered by long range magnetic order, but that has not been used in this project.

Neutron Powder Diffraction (NPD) data were collected via the HRPD Xpress route on the High-Resolution Powder Diffraction (HRPD) beamline at ISIS (Rutherford Appleton Laboratory). Bulk samples were loaded into 6 mm diameter vanadium cans (the lithiated sample was loaded in Ar in a glovebox and the can was then sealed with indium wire).

### 2.2.3 Rietveld Refinements

This is a whole pattern fitting technique which uses a least squares method to refine parameters (both structural and instrumental) to give the best fit of a calculated diffraction pattern to the experimental data.<sup>38</sup> In this project, Rietveld refinements were carried out using the TOPAS Academic Software.<sup>39</sup> For data collected in chapter 3, full Rietveld refinements were carried out for NPD data, refining peak shape, lattice parameters, atomic coordinates (as allowed by symmetry) and atomic displacement parameters. For PXRD data collected in chapters 4 to 5, only zero point, peak shape, unit cell parameters and phase fractions were refined. An important statistic obtained from Rietveld refinements is the weighted profile *R*-factor,  $R_{wp}$ , which tells us how well the experimental pattern is fitted to the calculated pattern. The mathematical expression which defines this value is shown below:

$$R_{wp} = \left\{ \frac{\sum w_i (y_i(obs) - y_i(calc))^2}{\sum w_i (y_i(obs))^2} \right\}^{1/2}$$

A refinement method used frequently throughout this project was the Pawley (Le Bail) technique. A Pawley fit is a whole pattern fitting method where observed peaks in a powder pattern are fitted without the use of a structural model. In this kind of fitting, the peak positions are constrained by the size of the unit cell. This process is usually used as a precursor to Rietveld fitting, as the best possible symmetry for the structure is obtained.<sup>40</sup>

ISODISTORT<sup>37</sup> was used to explore possible structural distortions.

### 2.2.4 Magnetic Susceptibility Measurements (SQUID)

A Superconducting Quantum Interference Device (SQUID) is a very sensitive instrument which allows the experimental determination of magnetic moments in a sample. A SQUID consists of superconducting loop containing insulating layers, which creates Josephson junc-

tions. A magnetic sample being analysed is moved up and down within the loop, producing an alternating magnetic flux.

In the temperature vs magnetisation plots, paramagnetism, ferromagnetism and antiferromagnetism are all portrayed differently. In the  $T$  vs  $\chi$  plot of a paramagnetic sample, the susceptibility increases at a steady rate as the temperature decreases. In a ferromagnetic sample, the susceptibility increases dramatically on cooling below the Curie temperature. On the other hand, in an antiferromagnetic sample, the susceptibility increases on cooling down to the Néel temperature, below which, the susceptibility decreases.

Field-cooled (FC) and zero-field-cooled (ZFC) magnetisation were measured on warming in an applied field of 0.1 T using a QD MPMS.

### **2.2.5 Density Functional theory (DFT)**

The results stated in this thesis are from calculations carried out by Dr Eric Bousquet and Dr Nick Bristowe.

The first principles calculations of the effective  $A^{2+}$  models were performed using the VASP<sup>41,42</sup> and ABINIT<sup>43</sup> packages both employed the PBEsol<sup>44</sup> exchange correlation functional and PAW pseudopotentials. The plane wave cut-off was set to 1000 eV and we used a  $5*5*3$  k-point mesh for the 18-atom cell, which was scaled proportionally for other size cells.

### **2.2.6 SEM/TEM measurements**

Scanning Electron Microscopy (SEM) analysis involves focusing a beam of electrons onto a sample in order to ascertain information about its surface topography. Electrons are fired from an electron gun through various lenses and apertures, which produces a focused electron beam that hits the sample surface. In SEM, two kinds of electron signals are given off, the Secondary Electron (SE) and the Backscattered Electron (BSE), which give complementary information about the sample. BSE imaging gives information about the compositional homogeneity of the sample, the more electron-dense the sample is in a certain area, the brighter it appears in the image. Secondary electrons, on the other hand, give information about the surface topography of the sample. SEM can also be paired with Energy-Dispersive X-Ray (EDX) analysis, which detects X-Rays emitted from the surface of the sample which are characteristic of the elements present. EDX can be used to determine the composition of a sample as well as for elemental mapping so that the elemental distribution on the surface can be seen.

By contrast, in Transmission Electron Microscopy (TEM) electrons pass through the sam-

ple, and can be diffracted, giving structural information. In this thesis, TEM was used in Chapter 3 to ascertain the local structure of one of the samples due to its complicated incommensurate modulation using Electron Diffraction.

SEM/EDX analysis was undertaken on a Hitachi S3400N microscope with an Oxford Instruments XMax80 EDX, with a  $80\text{mm}^2$  beam and analysed on the INCA software. Acceleration voltage was 20 kV.

Selected area electron diffraction (SAED) patterns were recorded on a CCD camera with a Philips CM20 transmission electron microscope operating at 200 kV.

## Chapter 3

# Tuning the octahedral tilts in the A-site deficient perovskite $\text{Nd}_{0.33}\text{NbO}_3$ through intercalation with $\text{Li}^+$ ions

### 3.1 Introduction

As mentioned in Chapter 1, A-site deficient perovskites are partially occupied layered structures, which are ordered in alternating partial occupancy and vacancy layers. The main focus of this chapter was on the  $\text{Nd}_{0.33}\text{NbO}_3$  structure, and its reductive intercalation reaction with  $\text{Li}^+$  ions.

$\text{Nd}_{0.33}\text{NbO}_3$  was reported to crystallise in the orthorhombic space group  $Cmmm$ , with  $a^-a^-c^0$  tilts.<sup>22</sup> In 1988, Nadiri reported the possibility of reductively intercalating  $\text{Li}^+$ , which in turn reduces the  $\text{Nb}^{5+}$  cations to  $\text{Nb}^{4+}$ .<sup>45</sup> The effect of this reduction is briefly reported, but there was little structural work done. This reductive intercalation reaction contrasts with the  $\text{La}_{2/3-x}\text{Li}_{3x}\text{TiO}_3$  solid solution in that the B site ions are partially reduced, whilst no  $\text{Ti}^{4+}$  ions are reduced in  $\text{La}_{2/3-x}\text{Li}_{3x}\text{TiO}_3$ .

The aim of this experiment was to understand the structural chemistry of the  $\text{Ln}_{0.33}\text{NbO}_3$  system and to investigate whether reduction through the intercalation of  $\text{Li}^+$  ions would change the octahedral tilting in the system.

## 3.2 Experimental

### 3.2.1 Synthesis of $\text{Nd}_{0.33}\text{NbO}_3$

Stoichiometric amounts of  $\text{Nd}_2\text{O}_3$  and  $\text{Nb}_2\text{O}_5$  were ground intimately in an agate pestle and mortar. The sample was then pressed as a pellet and heated at  $1000^\circ\text{C}$  for 12 h and then at  $1300^\circ\text{C}$  for 12 h several times (with intermittent grinding) to prepare  $\text{Nd}_{0.33}\text{NbO}_3$ . The sample was then analysed using PXRd and other characterisation methods as discussed in Chapter 2.

### 3.2.2 Reductive Intercalation to form $\text{Li}_x\text{Nd}_{0.33}\text{NbO}_3$

This was done in collaboration with Dr E. R. Clark.  $\text{Nd}_{0.33}\text{NbO}_3$  (2 g, 10.6 mmol) was transferred into a Schlenk flask and placed under vacuum for 1 minute to degas, after which the flask was refilled with Ar and nBuLi (80 cm<sup>3</sup>, 1.6 M in a mixture of hexanes, 128 mmol) was added to the stirring solid, forming a dark blue suspension which was stirred at room temperature for a week. Due to the air sensitivity of the sample, all handling was done in an Ar-filled glovebox, and Powder X-Ray Diffraction (PXRd) data were collected in an Ar-filled sealed sample holder.

### 3.2.3 Iodometric Titrations

To determine the lithium content in  $\text{Li}_x\text{Nd}_{0.33}\text{NbO}_3$ , iodometric titrations were done.  $\text{I}_2$  solution (0.217 g,  $8.5 \times 10^{-4}$  mols) in dry acetonitrile (15 ml) were added to  $\text{Li}_x\text{Nd}_{0.33}\text{NbO}_3$  (0.3 g,  $1.57 \times 10^{-3}$  mols) under argon and left to stir for 12 h under argon. The solution was then diluted to 0.05 dm<sup>3</sup> and titrated with  $\text{Na}_2\text{S}_2\text{O}_3$  (0.02 M). A starch indicator was used so that the end point could be identified.

## 3.3 Complementary Techniques

### 3.3.1 SQUID Magnetometry

Field-cooled (FC) and zero-field-cooled (ZFC) magnetisation were measured on warming in an applied field of 0.1 T using a QD MPMS.

### 3.3.2 Density Functional Theory

DFT calculations were carried out by Dr N. C. Bristowe and Dr E. Bousquet. See section 2.2.5 for more details.

### 3.3.3 Electron Diffraction (ED)

This was carried out by Dr J. Hadermann at the University of Antwerp.

See chapter 2 for more details on analytical methodology.

## 3.4 Results and Discussion

### 3.4.1 Synthesis and initial characterisation of $\text{Nd}_{0.33}\text{NbO}_3$ and $\text{Li}_x\text{Nd}_{0.33}\text{NbO}_3$

The starting oxide  $\text{Nd}_{0.33}\text{NbO}_3$  prepared was consistent with the structure reported by Roudeau in 2007.<sup>22,28</sup> After the initial heating there were impurities which were identified as unreacted  $\text{Nd}_2\text{O}_3$  and  $\text{Nb}_2\text{O}_5$  in the PXRD pattern, as well as Weberite-like phases, such as  $\text{NdNbO}_4$  and  $\text{Nd}_3\text{NbO}_7$ . Upon further heating, the impurities decreased enough to give a pure bulk sample. Rietveld refinements (See figure 3.1a) suggested that the unit cell parameters were similar to those reported in literature.<sup>28</sup>

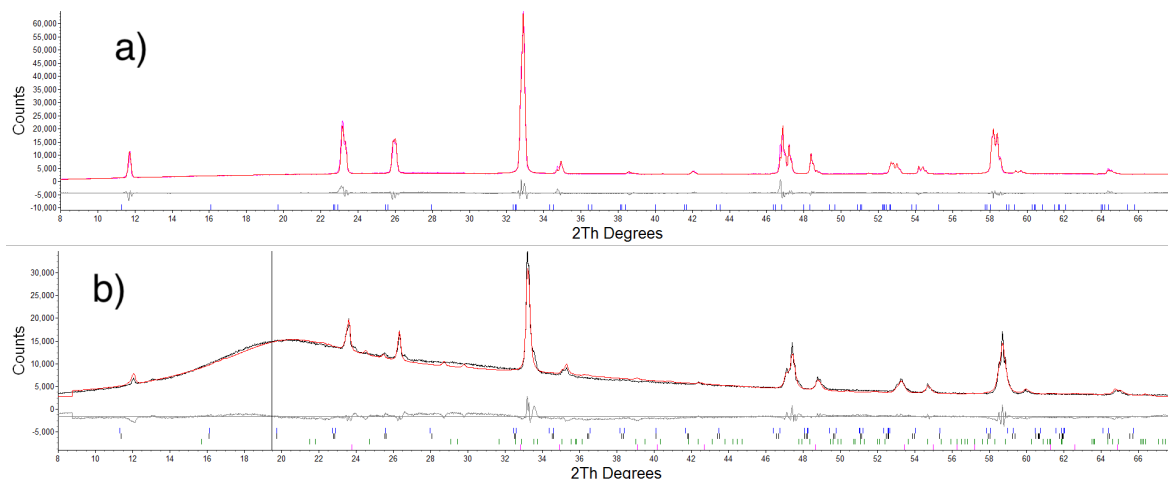
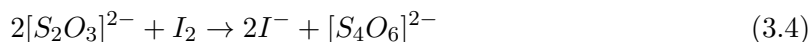


Figure 3.1: (a) Rietveld Refinement profile using the PXRD data of  $\text{Nd}_{0.33}\text{NbO}_3$  fit to  $Cmmm$  symmetry ( $a = 7.814520(9) \text{ \AA}$ ,  $b = 7.762557(9) \text{ \AA}$ ,  $c = 7.838586(9) \text{ \AA}$ ,  $R_{wp} = 5.821\%$ ) and (b)  $\text{Li}_x\text{Nd}_{0.33}\text{NbO}_3$  fit to  $P4/mmm$  symmetry ( $a = 7.767825(2)$ ,  $7.766895(2)$  and  $c = 7.824828(4)$ .  $R_{wp} = 5.575\%$ )

PXRD data for  $\text{Li}_x\text{Nd}_{0.33}\text{NbO}_3$  (see Figure 3.1b) were collected in an air-sensitive sample holder that gave an increased background to the data. Again, the main peaks were similar to those observed in  $\text{Nd}_{0.33}\text{NbO}_3$ , consistent with an  $A$ -site ordered perovskite structure with small traces of impurities, such as  $\text{LiCl}$ ,  $\text{LiNdO}_2$  and  $\text{LiNbO}_3$  also present.

Iodometric titrations were used to determine the number of moles of Li per formula unit in  $\text{Li}_x\text{Nd}_{0.33}\text{NbO}_3$ . The number of moles calculated based on the titration was 0.34, meaning that all of the vacancies in the structure had been filled with Li, indicating a successful

intercalation reaction had taken place. The redox half equations (equations 3.1 - 3.3) were as follows, as well as the redox reaction for the iodometric titration (equation 3.4):



As can be seen from the equations above,  $Li_xNd_{0.33}NbO_3$  reduced some of the iodine (in excess) during the titration to iodide; the remaining iodine in the solution was titrated with thiosulfate in order to determine the concentration of  $Li^+$  ions in  $Li_xNd_{0.33}NbO_3$ .

We note that the presence of soluble Li-containing impurities would affect the calculated moles of lithium per formula unit, however, refinements using NPD data (see below) indicate negligible amounts of these impurities in the sample and so negligible impact on the calculated lithium content.

### 3.4.2 Characterisation of $Nd_{0.33}NbO_3$ by NPD

To confirm the tilts present in  $Nd_{0.33}NbO_3$  using NPD, the peaks not fitted by the  $P4/mmm$  model were investigated (Figure 3.2a). A Pawley refinement using the P222 unit cell shows these additional reflections at 113000  $\mu s$ , 87000  $\mu s$ , and 63000  $\mu s$  (d-spacing of 2.35 Å, 1.79 Å and 1.32 Å respectively) that result from the lowering of symmetry (due to octahedral tilts) that are not indexed by the  $P4/mmm$  model.

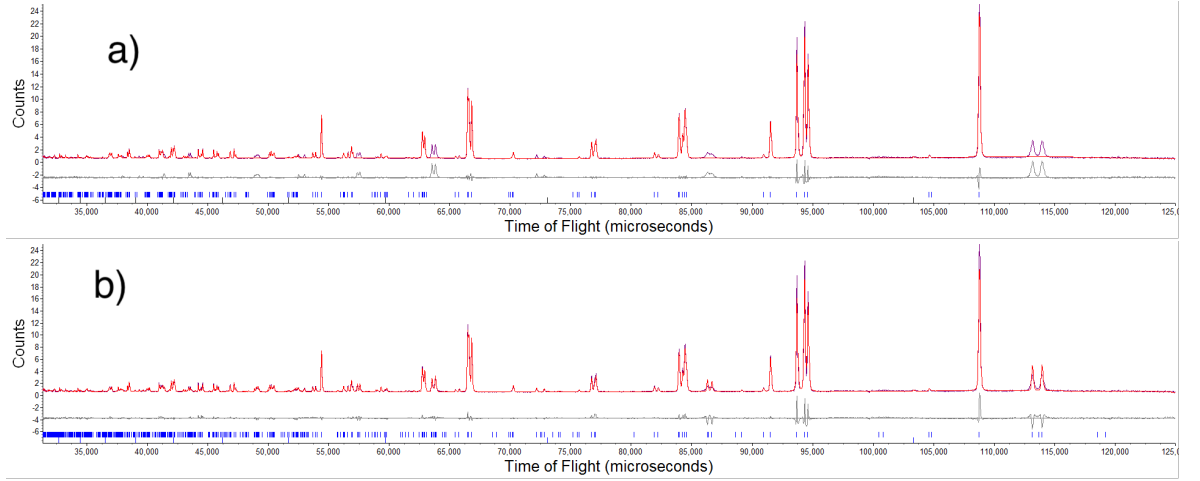


Figure 3.2: (a) A *LeBail* fit to the *P222* space group to fit room temperature NPD data ( $168^\circ$  bank) collected for  $\text{Nd}_{0.33}\text{NbO}_3$  ( $a = 7.814520$  (4)  $\text{\AA}$ ,  $b = 7.762557$  (5)  $\text{\AA}$ ,  $c = 7.838586$  (3)  $\text{\AA}$ ,  $R_{wp} = 5.821\%$ )(top) and (b) *Rietveld* refinement profile fit to the *Cmmm* space group using NPD data for  $\text{Nd}_{0.33}\text{NbO}_3$  ( $a = 7.81442$ (5)  $\text{\AA}$ ,  $b = 7.76249$ (5)  $\text{\AA}$ ,  $c = 7.83859$ (5)  $\text{\AA}$ ,  $R_{wp} = 4.45\%$ ) where the superstructure peaks have been fitted (bottom)

Symmetry analysis using ISODISTORT mapped out unit cell dimensions and symmetries expected for *A*-site ordered perovskites with different combinations (see figure 3.3) of tilts. Pawley refinements using these different models indicated that a model of *Cmmm* symmetry (which allows for  $a^-b^0c^0$  tilts, M5- irrep) gave a good fit to the data. Refined lattice parameters and bond lengths (see Table 3.1) are given as well as the structure (see Figure 3.4) are shown.

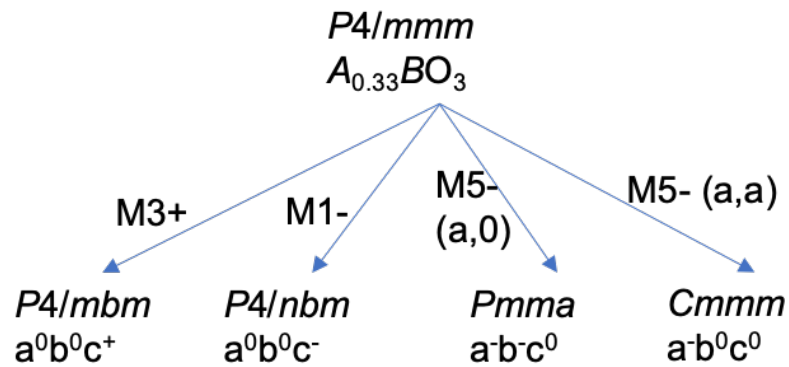


Figure 3.3: *Symmetry analysis from ISODISTORT showing range of tilt distortions that  $\text{Nd}_{0.33}\text{NbO}_3$  can undergo with respect to the *P4/mmm* space group*

We note that the peak shape for the superstructure reflections is not well fitted with these peaks being slightly broader than the main phase peaks. This could indicate a shorter correlation length of octahedral tilts than of the cation sublattice. This characterisation of the

$\text{Nd}_{0.33}\text{NbO}_3$  starting oxide gives a reference with which to compare the lithiated sample.

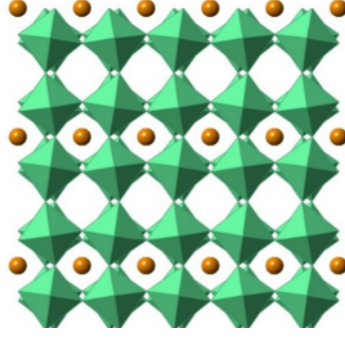


Figure 3.4: A crystallographic representation of the starting oxide  $\text{Nd}_{0.33}\text{NbO}_3$ , with Nd atoms in orange and  $\text{NbO}_6$  octahedra in green

Table 3.1: A table showing the refined bond lengths in  $\text{Nd}_{0.33}\text{NbO}_3$  in orthorhombic  $Cmmm$  symmetry

Bond	Length ( $\text{\AA}$ )	Bond	Length ( $\text{\AA}$ )
Nd – O(1)	$2 \times 2.527(2)$	Nb – O(2)	1.8943(8)
Nd – O(1)	$2 \times 2.992(2)$	Nb – O(4)	1.957(1)
Nd – O(3)	$2 \times 2.539(2)$	Nb – O(5)	$2 \times 1.9684(1)$
Nd – O(5)	$4 \times 2.6500(8)$	Nb – O(3)	1.983(1)
Nd – O(4)	$2 \times 2.870(1)$	Nb – O(1)	2.0680(8)

### 3.4.3 Characterisation of $\text{Li}_x\text{Nd}_{0.33}\text{NbO}_3$ by NPD

The main peaks observed in the high resolution NPD pattern for  $\text{Li}_x\text{Nd}_{0.33}\text{NbO}_3$  (See Figure 3.5) could be indexed by the untilted,  $A$ -site ordered model of  $P4/mmm$  symmetry, as reported by Nadiri *et al.*<sup>45</sup> However, broadening, as well as a decrease in intensity of the additional peaks was observed at 112000  $\mu\text{s}$ , 91000  $\mu\text{s}$ , and 63000  $\mu\text{s}$  (d-spacing of 2.35 $\text{\AA}$ , 1.79  $\text{\AA}$  and 1.32  $\text{\AA}$  respectively). These peaks could not be indexed using commensurate unit cells, or any impurity phases.

This broadening of the superstructure peaks comes from disorder, or possibly even short-range ordering from within the structure. A possible reason for this disorder is that there may be some incommensurately modulated O-Li sublattices forming across the entire structure in a disordered fashion, causing the additional peaks in the pattern to broaden.

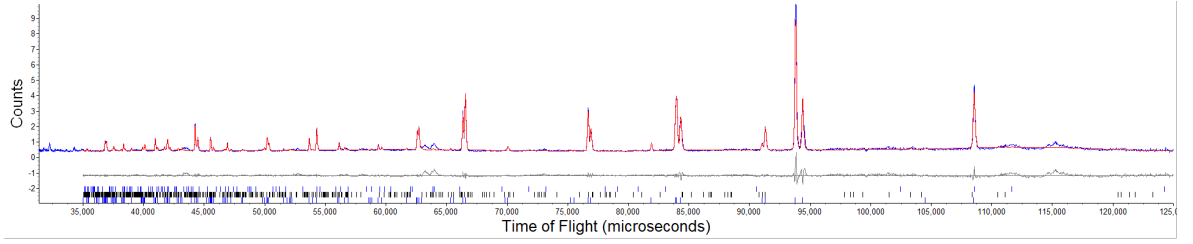


Figure 3.5: A *LeBail* fit to the *P222* space group to fit room temperature NPD data ( $168^\circ$  bank) collected for  $\text{Li}_{0.34}\text{Nd}_{0.33}\text{NbO}_3$  ( $a = 7.814520$  (4) Å,  $b = 7.762557$  (5) Å,  $c = 7.838586$  (4) Å,  $R_{wp} = 5.821\%$ )

To further understand the cause of these broadened superstructure peaks, a more local probe (such as electron diffraction and solid-state NMR) is needed. This is because, with electron diffraction, it will become easier to see where the diffuse scattering is within the structure, and if/how it is ordered, as well as the general ordering of the structure. Solid-state NMR on the other hand, is used to see the local environments of individual elements, and what they are bound to within the structure.

Niobium and lithium Solid-State NMR will be done to further understand the local environments of these elements within the structure. An issue that may be faced with this, is that upon intercalation, the  $\text{Li}^+$  ion donates an electron to the  $d^0 \text{Nb}^{5+}$  cation, causing it to become paramagnetic, meaning that there may be a broadening of the peaks in the pattern.

#### 3.4.4 Electron Diffraction of $\text{Li}_x\text{Nd}_{0.33}\text{NbO}_3$

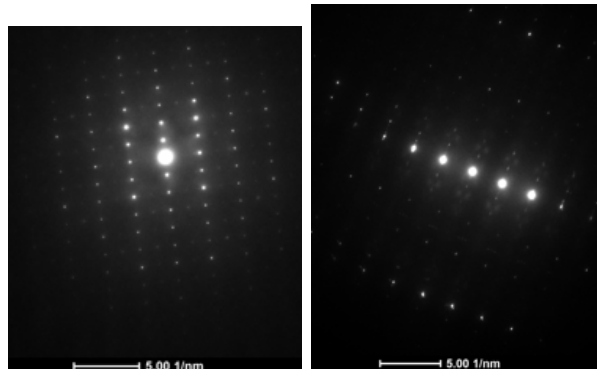


Figure 3.6: A figure showing the Electron Diffraction patterns for  $\text{Li}_x\text{Nd}_{0.33}\text{NbO}_3$  down the  $[100]$  zone axis. The pattern on the left shows the Bragg reflections, whereas the figure on the right is a close up of the zone axis showing the diffuse scattering in the structure

Preliminary characterisation using electron diffraction data collected down the  $[100]$  zone axis (Figure 3.6) reveals clear, sharp spots consistent with the parent  $P4/mmm$  model. However, incommensurate reflections (like those seen in  $\text{Li}_{3x}\text{Nd}_{2/3-x}\text{TiO}_3$ <sup>30</sup>) are observed (see Figure

3.6, right). In addition, some more diffuse scatter is observed in these electron diffraction images (e.g. off-axis "fuzzy" spots in the right panel of Figure 3.6). This is consistent with the broad superstructure peaks observed in NPD data and as noted above, this may reflect a more complex O/Li sublattice, and further work is needed to fully understand this.

### 3.4.5 Magnetic Susceptibility measurements

Magnetic susceptibility measurements (see Figure 3.7) collected in an applied field of 0.1 T show that both materials remain paramagnetic down to 2 K. Graphs showing the inverse susceptibility against temperature show a reasonable agreement with the Curie-Weiss law when  $T \geq 150$  K.

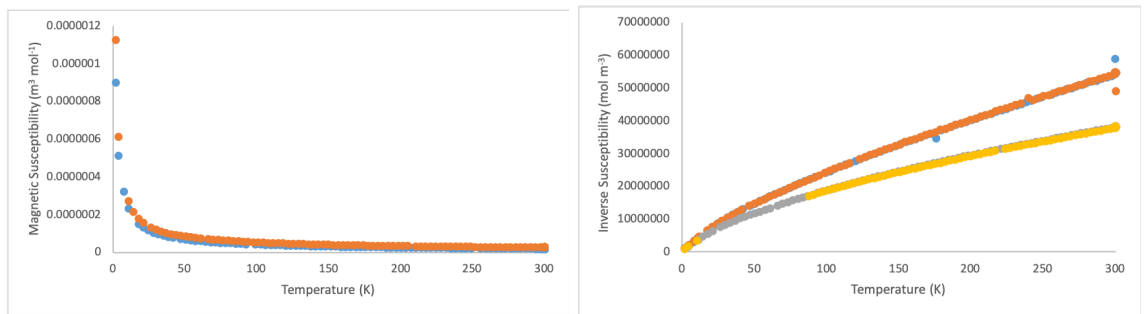


Figure 3.7:  $T$  vs  $\chi_m$  data for both  $Nd_{0.33}NbO_3$  and  $Li_{0.34}Nd_{0.33}NbO_3$  (left),  $T$  vs  $\chi^{-1}$  for  $Nd_{0.33}NbO_3$  and  $Li_{0.34}Nd_{0.33}NbO_3$  (blue and orange correspond to  $Nd_{0.33}NbO_3$  ZFC and FC, respectively. Grey and yellow correspond to  $Li_{0.34}Nd_{0.33}NbO_3$  ZFC and FC respectively).

For  $Nd_{0.33}NbO_3$ , the paramagnetic moment from this data (see Figure 3.7) suggests a moment of  $\mu = 2.09 \mu_\beta$  per formula unit ( $3.618 \mu_\beta$  per  $Nd^{3+}$  ion). Expected moment calculations were done using Russell-Saunders coupling scheme, where  $S = 3/2$ ,  $L = 6$  and  $J = 9/2$ , meaning that the  $Nd^{3+}$  ( $4f^3$ ) is in fact a  $^4I_{9/2}$  ion.<sup>?</sup> The expected moment was calculated to be  $\mu = 2.10 \mu_\beta$  which was in good agreement to the experimentally obtained moment. The Weiss temperature ( $\theta_{CW}$ ) calculated from the plots was -79 K.

For  $Li_{0.34}Nd_{0.33}NbO_3$ , a similar Curie-Weiss approach was taken, which suggests a moment of  $\mu = 2.68 \mu_\beta$  per formula unit. This increased paramagnetic moment is a result of the reduction of approximately a third of the  $Nb^{5+}$  ions to the paramagnetic  $4d^1 Nb^{4+}$  ion. Whilst most of the moment per formula unit results from the  $Nd^{3+}$  ions, the data suggest a moment of  $2.88 \mu_\beta$  per  $Nb^{4+}$  ion. The Weiss temperature ( $\theta_{CW}$ ) obtained was -136 K.

### 3.4.6 Density Functional Theory

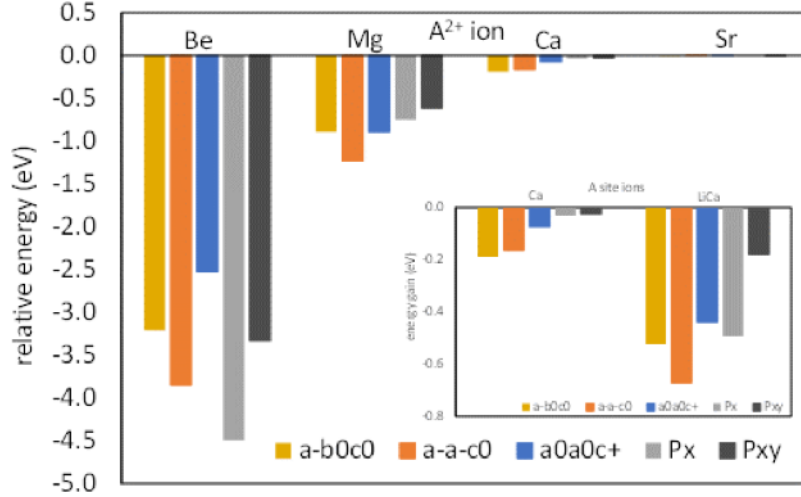


Figure 3.8: *Energies of possible lower symmetry structures (relative to the ideal  $P4/mmm$  model) for the  $A_{0.5}^{2+}NbO_3$  series. Relative energies are given per 9 atom chemical formula unit. Stabilisation energies for the lithiated sample are shown inset.*

To overcome the difficulty of building models for DFT calculations with alternating layers of sites which are only two-thirds occupied, by  $Ln^{3+}$  ions, an alternate series of models, with alternating layers of fully occupied  $A^{2+}$  ions were used. The results (See Figure 3.8) suggest that, as the divalent cation becomes smaller, polar distortions give larger energy gains than octahedral tilt distortions. This is consistent with the polar crystal structures reported for  $Ln_{0.33}TaO_3$  with smaller  $Ln$  cations (See Table 1.1).<sup>23</sup>

Calculations on the Li-inserted model (inset) show a significant increase in energy gain for the distortions considered, and the largest energy gain from the  $a^-a^-c^0$  tilts. Such tilting over a long range would give superstructure reflections at similar time-of-flight to the broad reflections observed, suggesting that this tilt system may be present, but only over shorter length scales.

## 3.5 Conclusions and Future Work

Both the non-lithiated and the lithiated samples were successfully synthesised and characterised. The analysis done on both samples shows the structure undergoes a change when some of the vacancies in the structure are occupied by  $Li^+$ . Unfortunately the ordering of  $Li^+$  within the structure is still mostly unknown. Theory suggests that upon lithiation, the energy gain from tilting within the structure increases.

### 3.5.1 Future Work

Solid-state NMR would be able to aid in the determination of the ordering of Li ions within the structure, as well as the origin of the incommensurate modulation in the structure. Something that would confirm the polar nature post-lithiation, would be to use second harmonic generation (SHG), which would show us whether or not the structure was non-centrosymmetric.

It would be interesting to explore the possibility of intercalating higher concentrations of Li ions: there have been reports that adding higher concentrations of Li tunes the electronic structure such that it becomes more metallic.<sup>46</sup> From our composition of  $\text{Li}_{0.34}\text{Nd}_{0.33}\text{NbO}_3$ , it should be possible to introduce more lithium into the structure to give a maximum lithium content of  $\text{Li}_{0.66}\text{Nd}_{0.33}\text{NbO}_3$  with lithium ions on all *A*-sites and it would be interesting to explore influence of lithium content per formula unit on the magnetic and electronic properties.

## Chapter 4

# Synthesis and characterisation of

# $\text{La}_4\text{Mg}_3\text{W}_3\text{O}_{18}$ and

# $\text{La}_{(4-x)}\text{Nd}_x\text{Mg}_3\text{W}_3\text{O}_{18}$ ( $0 \leq x \leq 2$ )

### 4.1 Introduction

Having explored the *A*-site deficient  $\text{Ln}_{0.33}\text{NbO}_3$  in Chapter 3, we were interested in the *B*-site ordered material  $\text{La}_4\text{Mg}_3\text{W}_3\text{O}_{18}$ . This was reported in 2005 by Khalyavin and analysed using PXRD which indicated that there was a checkerboard ordering of the  $\text{Mg}^{2+}$  and  $\text{W}^{6+}$  on the *B*-sites. This is due to the fact that there is a large charge and ionic radius difference between the two cations (0.72 Å vs 0.6 Å for 6-coordinate  $\text{Mg}^{2+}$  and  $\text{W}^{6+}$ , respectively). This checkerboard *B*-site ordering can be described by the  $\text{R1+}$  irrep (compared to the  $\text{Pm}\bar{3}m$  ideal structure).

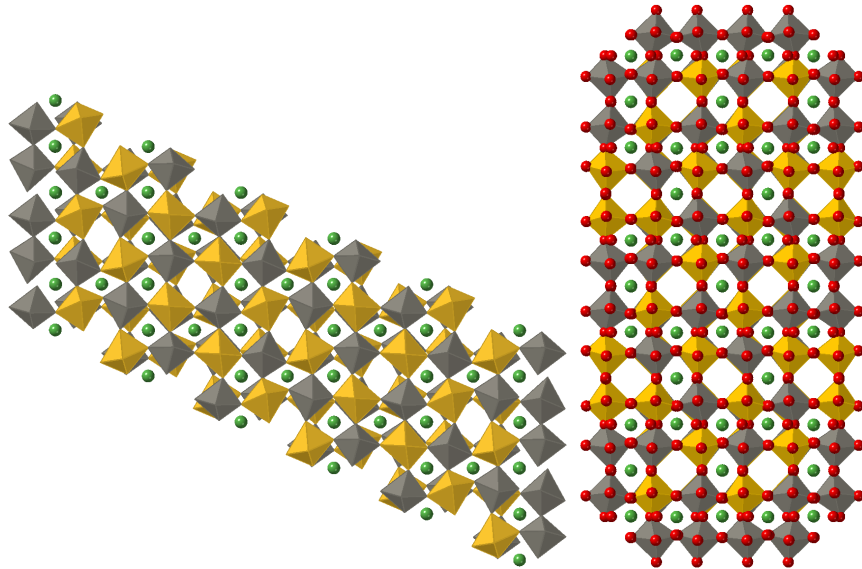


Figure 4.1: A diagram showing both crystal structures for  $\text{La}_4\text{Mg}_3\text{W}_3\text{O}_{18}$ , with the left hand figure showing the lower symmetry  $C2/m$  structure, and the figure on the right showing the higher temperature, higher symmetry  $Ibam$  structure

In addition to  $B$ -site ordering, the  $A$ -sites are not fully occupied, and  $\text{La}^{3+}$  ions adopt a complicated ordering pattern (see Figure 4.1), in which some sites are fully occupied, some are partially occupied and others vacant. This ordering is described using the  $Z4$  irrep (compared to the  $\text{Pm}\bar{3}m$  space group). This combined  $A$ - and  $B$ -site ordering lowers the symmetry of the system to  $Ibam$ , and Khalyavin *et al.* observed this phase at high temperature.<sup>35</sup> On cooling, the  $\text{La}_4\text{Mg}_3\text{W}_3\text{O}_{18}$  undergoes a phase transition to the  $C2/m$  structure (through the  $R4+$  distortion) which also allows the  $a^-b^0c^0$  tilts. Both of these structures are centrosymmetric, however, if a further tilt ( $a^0b^0c^+$ ,  $M3+$  irrep) is induced in the  $C2/m$  structure, inversion symmetry would break and give a non-centrosymmetric  $C2$  structure.

Our aim here was to explore the compositional flexibility of  $\text{La}_4\text{Mg}_3\text{W}_3\text{O}_{18}$  and to see whether the structure, as well as the properties could be tuned. In this chapter,  $A$ -site doping in  $\text{La}_{(4-x)}\text{Nd}_x\text{Mg}_3\text{W}_3\text{O}_{18}$  is considered, and in the following chapter,  $B$ -site dopants are explored.

## 4.2 Synthesis of $\text{La}_4\text{Mg}_3\text{W}_3\text{O}_{18}$ and $\text{La}_{(4-x)}\text{Nd}_x\text{Mg}_3\text{W}_3\text{O}_{18}$ ( $0 \leq x \leq 2$ )

Stoichiometric amounts of  $\text{La}_2\text{O}_3$ ,  $\text{Nd}_2\text{O}_3$ ,  $\text{MgO}$  and  $\text{WO}_3$  were ground intimately using an agate pestle and mortar. The sample was then pressed as a pellet and heated at  $1350^\circ\text{C}$  for 24 h to prepare both  $\text{La}_4\text{Mg}_3\text{W}_3\text{O}_{18}$  and  $\text{La}_{(4-x)}\text{Nd}_x\text{Mg}_3\text{W}_3\text{O}_{18}$  where  $0 \leq x \leq 2$ .

Samples were also characterised by PXRD, SQUID magnetometry and through Rietveld refinements (see Chapter 2 for more details).

### 4.2.1 SEM/EDX analysis

SEM/EDX analysis was done on a Hitachi S3400N microscope with an Oxford Instruments XMax80 EDX, with a 80mm<sup>2</sup> beam and analysed on the INCA software. The acceleration voltage was 20 kV.

## 4.3 Results and Discussion

### 4.3.1 La<sub>4</sub>Mg<sub>3</sub>W<sub>3</sub>O<sub>18</sub>

#### Powder X-Ray Diffraction

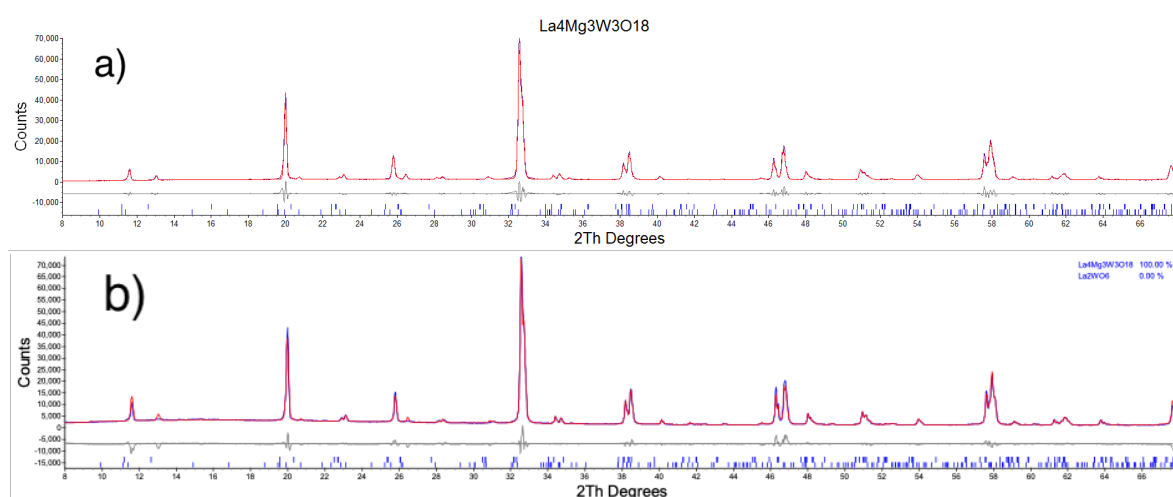


Figure 4.2: Rietveld refinement profile using PXRD data of the unquenched La<sub>4</sub>Mg<sub>3</sub>W<sub>3</sub>O<sub>18</sub>, with the red, blue and grey lines showing experimental, calculated and difference patterns respectively fit to *C2/m* symmetry ( $a = 17.643191(2) \text{ \AA}$ ,  $b = 7.824886(4) \text{ \AA}$ ,  $c = 7.824676(2) \text{ \AA}$ ,  $\beta = 116.36421^\circ (4)$ ,  $R_{wp} = 12.517\%$ ) and the Rietveld refinement profile using PXRD data of the quenched La<sub>4</sub>Mg<sub>3</sub>W<sub>3</sub>O<sub>18</sub> post-quenching, with the red, blue and grey lines showing experimental, calculated and difference patterns respectively, fit to *Ibam* symmetry ( $a = 7.819604 \text{ \AA}$ ,  $b = 15.802158 \text{ \AA}$ ,  $c = 7.831448 \text{ \AA}$ ,  $R_{wp} = 9.431\%$ ). Upper ticks correspond to the pure phases and the bottom ticks correspond to the La<sub>2</sub>WO<sub>6</sub> impurity (Le Bail fit)

Room temperature PXRD patterns (Figure 4.2a) show there is a good fit to the *C2/m* structure reported in literature.<sup>35</sup> As can be seen from the PXRD pattern, an additional peak is observed at 28° 2θ which is due to La<sub>2</sub>WO<sub>6</sub>. Unfortunately, whilst this additional peak could be fitted by a Pawley phase, it was not fitted by a Rietveld phase. This additional peak

could result from the main phase being lanthanum-deficient. An attempt was made to make a more *A*-site deficient structure,  $\text{La}_{2.5}\text{Mg}_{0.5}\text{W}_{0.5}\text{O}_{12}$ . However, characterisation by PXRD (See fig 4.3) showed that the intensity of the  $\text{La}_2\text{WO}_6$  peak at  $28^\circ 2\theta$  had not decreased, ruling out deficiency as a reason.

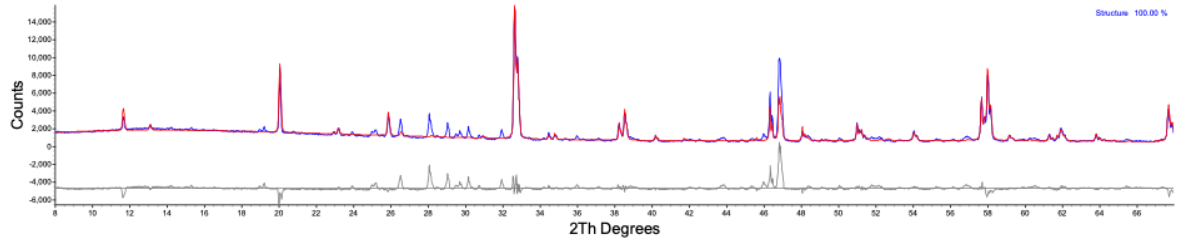


Figure 4.3: A diagram showing the PXRD pattern of the deficient  $\text{La}_{2.5}\text{Mg}_{0.5}\text{W}_{0.5}\text{O}_{12}$  fit to the  $C2/m$  space group ( $a = 7.818048(9)$ ,  $b = 15.811272(3)$ ,  $c = 7.828363(8)$ ,  $R_{wp} = 16.07\%$ )

To attempt to see the phase transition reported at 700 K, a pellet of  $\text{La}_4\text{Mg}_3\text{W}_3\text{O}_{18}$  was quenched from the furnace at  $1100^\circ\text{C}$ . As can be seen from the PXRD pattern obtained (see Figure 4.2b), the product had indeed crystallised in the higher symmetry orthorhombic *Ibam* structure. The main difference between the patterns for the two symmetries is the peak at approximately  $13^\circ 2\theta$ . In the pattern for  $C2/m$  symmetry, the peak has observed intensity, whereas upon transition *Ibam*, a peak is predicted, but no intensity is observed.

#### 4.3.2 $\text{La}_{4-x}\text{Nd}_x\text{Mg}_3\text{W}_3\text{O}_{18}$

The potential solid solution  $\text{La}_{4-x}\text{Nd}_x\text{Mg}_3\text{W}_3\text{O}_{18}$  was investigated. Initial PXRD analysis indicated that for samples in the  $0 \leq x \leq 2$  range, the main peaks were consistent with the  $C2/m$  model reported for  $\text{La}_4\text{Mg}_3\text{W}_3\text{O}_{18}$  (see figure 4.2). For  $x \geq 2$ , impurity peaks, attributable to  $\text{NdWO}_4$  were observed, as well as peaks for the unreacted reagents.

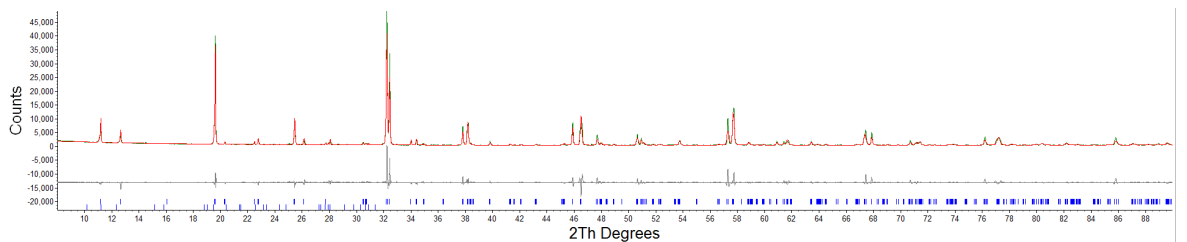


Figure 4.4: A diagram showing the PXRD pattern of the highest doped concentration  $\text{La}_2\text{Nd}_2\text{Mg}_3\text{W}_3\text{O}_{18}$ , with the pink, blue and grey lines showing experimental, calculated and difference patterns respectively, fit to  $C2/m$  symmetry ( $a = 17.63347(3) \text{ \AA}$ ,  $b = 7.787392(8) \text{ \AA}$ ,  $c = 7.808331(8) \text{ \AA}$ ,  $\beta = 116.3326(4)^\circ$ ,  $V = 962.696(4) \text{ \AA}^3$ ,  $R_{wp} = 15.886\%$ ). Upper ticks correspond to the pure Nd doped phase and the bottom ticks correspond to the  $\text{La}_2\text{WO}_6$  impurity (Le Bail fit)

Unit cell parameters obtained from Rietveld refinements using the PXRD data suggest a smooth decrease in unit cell volume with increasing Nd content (see Figure 4.6(d)), consistent with the smaller ionic radius of  $\text{Nd}^{3+}$  compared to  $\text{La}^{3+}$  (1.36 Å for  $\text{La}^{3+}$  and 1.41 Å for  $\text{Nd}^{3+}$ ).<sup>47</sup> The main difference between the patterns of the undoped and the doped compounds, is that there is an increase in the splitting of the peak at  $32^\circ 2\theta$ , with increasing Nd content (see Figure 4.5).

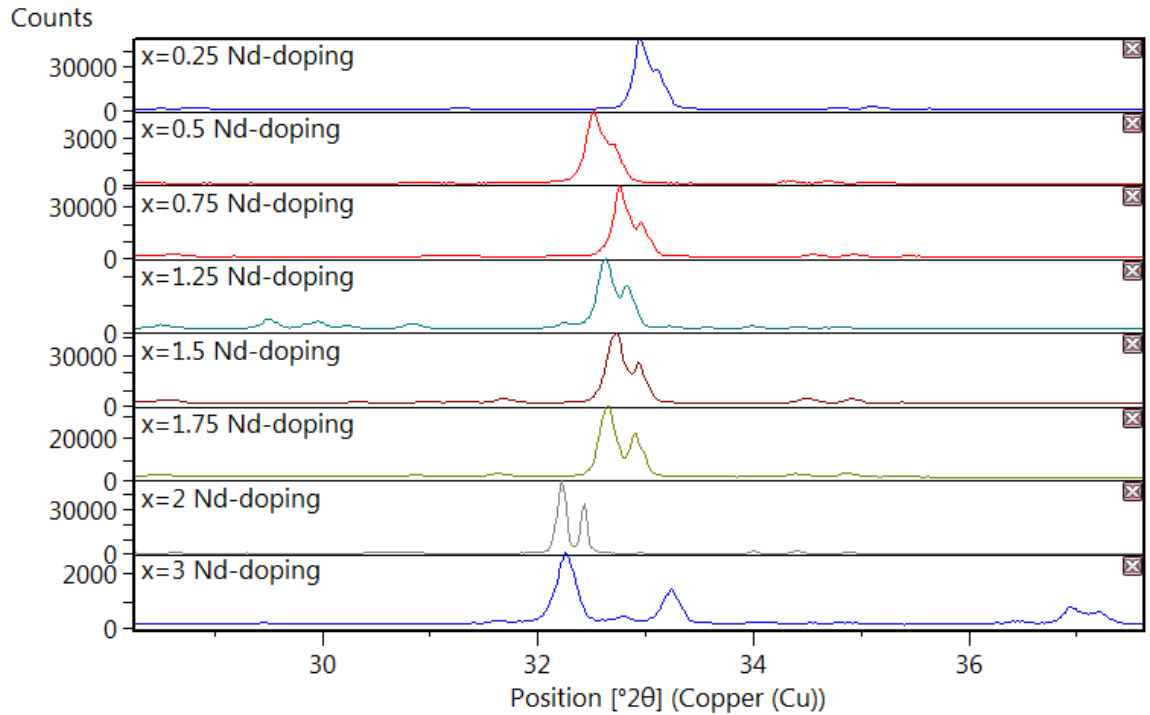


Figure 4.5: A diagram showing the evolution of the splitting of the main phase  $[2,-2,-2]$  peak at  $32^\circ 2\theta$  in the  $\text{La}_{4-x}\text{Nd}_x\text{Mg}_3\text{W}_3\text{O}_{18}$  solid solution

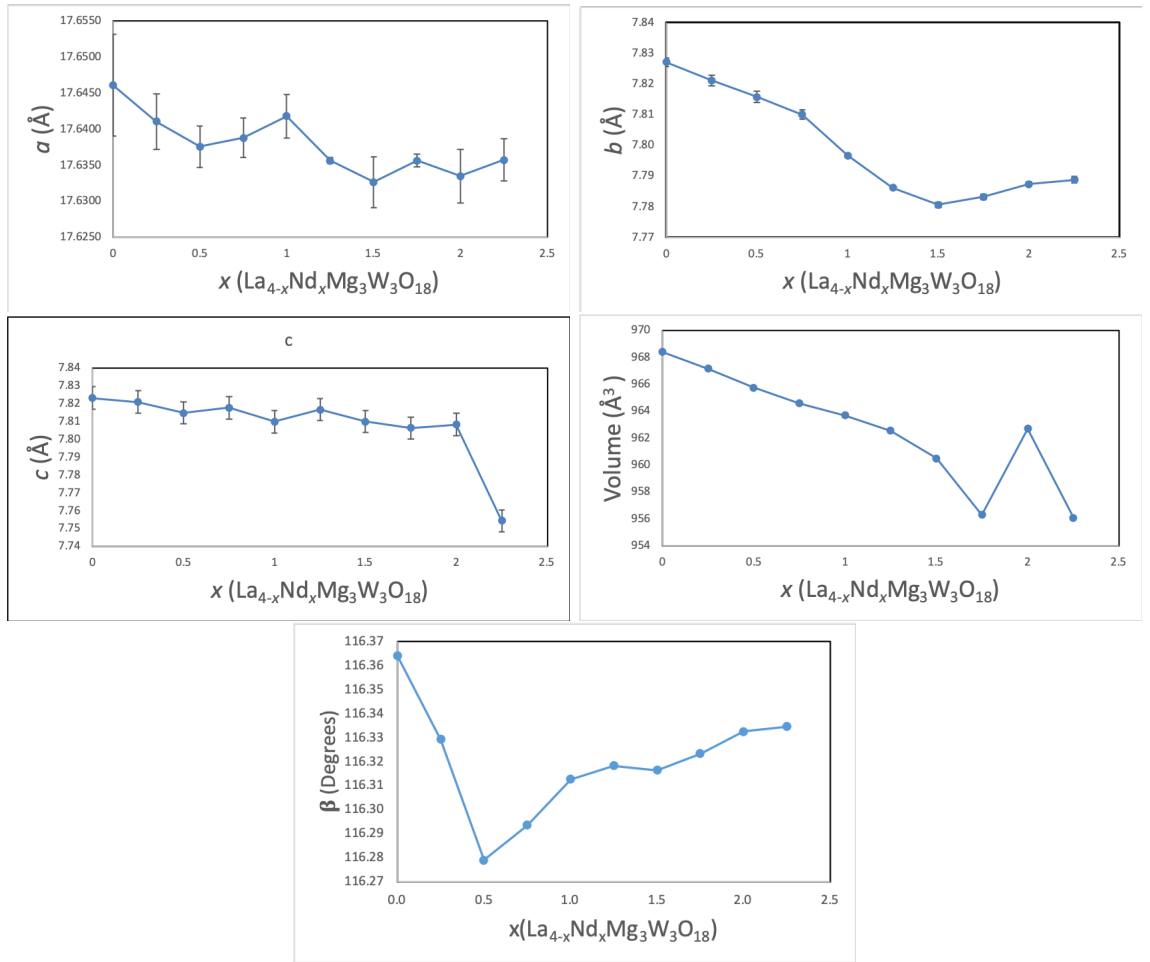


Figure 4.6: A diagram showing the lattice parameter plots for the  $\text{La}_{4-x}\text{Nd}_x\text{Mg}_3\text{W}_3\text{O}_{18}$  solid solution for the  $C2/m$  space group

These results suggest that some  $\text{La}^{3+}$  cations can be replaced by  $\text{Nd}^{3+}$  in  $\text{La}_4\text{Mg}_3\text{W}_3\text{O}_{18}$  but that the proposed solid solution is limited to  $x \leq 1.5$  (see Figure 4.6). The greatest decrease is in the  $b$  lattice parameter; this is due to contraction of the cell along that axis when the smaller cation is introduced to the structure.

SEM and EDX measurements were also carried out on this sample to look at the surface and the elemental composition of the sample. As can be seen from the BSE images (see Appendix Figure 2), the powder was inhomogeneous (as shown by the contrast in brightness in the BSE images). However, elemental mapping (see Appendix Figure 4.7) showed that the distribution of La and Nd was even throughout the sample surface. Further analysis is needed to identify the composition of the impurity phases. EDX analysis of an area indicated a ratio of La:Nd:Mg:W of 1.9(1):1.9(1):3.0(1):3.2(1) (see Table 2) consistent with the target stoichiometry of  $\text{La}_2\text{Nd}_2\text{Mg}_3\text{W}_3\text{O}_{18}$ .

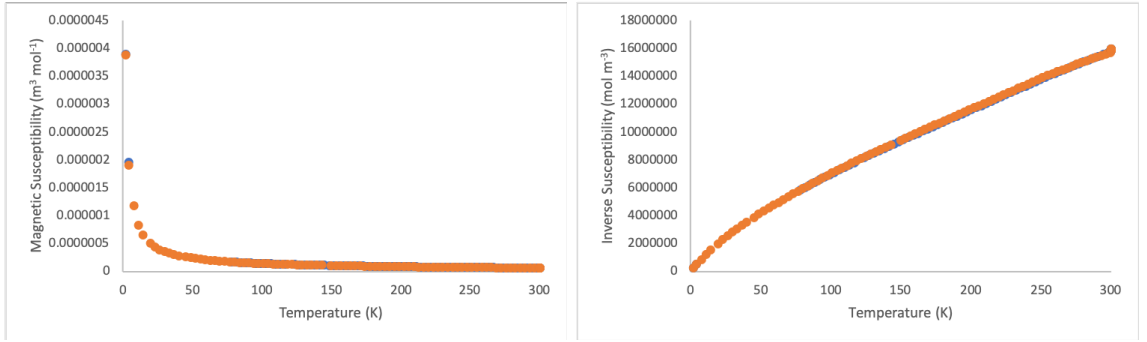


Figure 4.7:  $T$  vs  $\chi_m$  and  $T$  vs  $\chi^{-1}$  data for  $\text{La}_2\text{Nd}_2\text{Mg}_3\text{W}_3\text{O}_{18}$  (blue and orange lines correspond to ZFC and FC respectively).

Magnetic susceptibility measurements were done on the highest concentration  $\text{La}_2\text{Nd}_2\text{Mg}_3\text{W}_3\text{O}_{18}$ . As can be seen from the susceptibility plots (Figure 4.7), the sample is paramagnetic down to 2 K. On the  $1/\chi$  plot, the sample shows Curie-Weiss behaviour when  $T \geq 150$  K, below which the plot starts to curve. There are some reasons for this. The effective magnetic moment ( $\mu_{eff}$ ) obtained for  $\text{La}_2\text{Nd}_2\text{Mg}_3\text{W}_3\text{O}_{18}$  was  $2.557 \mu_B$  ( $3.618 \mu_B$  per  $\text{Nd}^{3+}$  ion) with a Weiss temperature  $\theta_{CW}$  of -59 K.

#### 4.4 Conclusions and Future work

$\text{La}_4\text{Mg}_3\text{W}_3\text{O}_{18}$  was successfully synthesised and characterised using the techniques detailed above. The PXRD pattern shows that the unquenched sample is of  $C2/m$  symmetry (consistent with literature). However, as could be seen from the PXRD patterns of both the unquenched and the quenched sample, there is a marked difference in the intensity of the peak at approximately  $13^\circ 2\theta$ , showing that the phase transition had taken place and the sample had crystallised in the higher symmetry  $Ibam$  structure, meaning that this high temperature, high symmetry could be isolated.

Attempts to introduce  $\text{Nd}^{3+}$  ions onto the  $\text{La}^{3+}$  site suggest that the solid solution is limited ( $x \leq 1.5$ ) and that  $\text{Nd}_4\text{Mg}_3\text{W}_3\text{O}_{18}$  could not be prepared (see Appendix Figure 1). This was surprising given that the difference between ionic radii is smaller than 15%.<sup>48</sup> This therefore shows that these  $B$ -site ordered,  $A$ -site deficient perovskites are relatively inflexible in terms of composition. Within the solution range ( $0 \leq x \leq 1.5$ ), the unit cell volume decreases, which is consistent with the ionic radii, and the monoclinic angle does not change systematically with Nd content.

#### 4.4.1 Future Work

It would be interesting to explore the  $C2/m$  to  $Ibam$  phase transition in these  $\text{La}_{4-x}\text{M}_x\text{Mg}_3\text{W}_3\text{O}_{18}$  (where M is other lanthanides or trivalent cations) through thermal and structural analyses (such as variable temperature PXRD and NPD, as well as DSC). It would also be interesting to investigate whether introducing smaller  $A$ -site cations on to the La site (which reduces the average tolerance factor from 0.956 for the hypothetical  $\text{La}(\text{Mg},\text{W})\text{O}_3$  to 0.944 for the hypothetical  $(\text{La}_{0.625}\text{Nd}_{0.375})(\text{Mg},\text{W})\text{O}_3$ ) would increase the temperature of the structural phase transition, as well as whether further structural distortions might occur during cooling, meaning low temperature PXRD is of interest.

## Chapter 5

# *B*-site doping of $\text{La}_4\text{Mg}_3\text{W}_3\text{O}_{18}$ with Cu/Zn and double *B*-site substitution with Fe/Mn and Ta

### 5.1 Introduction

Continuing from Chapter 4, this chapter focuses on *B*-site substitution in  $\text{La}_4\text{Mg}_3\text{W}_3\text{O}_{18}$  in an attempt to tune the structure and properties. Substitution with  $d^{10}$   $\text{Zn}^{2+}$  was attempted, with the hope that the more flexible coordination environment of this non-transition metal cation would be ideal for the substitution for the s-block  $\text{Mg}^{2+}$  cation. Magnetic ions, including  $\text{Cu}^{2+}$ ,  $\text{Fe}^{3+}$  and  $\text{Mn}^{3+}$  were also considered for substitution due to their similar ionic radii. However, in order to balance the structure when introducing the trivalent  $\text{Mn}^{3+}$  and  $\text{Fe}^{3+}$ , a double substitution was attempted, with  $\text{Ta}^{5+}$  replacing  $\text{W}^{6+}$ .

### 5.2 Experimental

#### 5.2.1 Cu/Zn-doped $\text{La}_4\text{Mg}_3\text{W}_3\text{O}_{18}$

Stoichiometric amounts of  $\text{La}_2\text{O}_3$ ,  $\text{CuO}$ ,  $\text{ZnO}$ ,  $\text{MgO}$ ,  $\text{WO}_3$  and  $\text{Ta}_2\text{O}_5$  were ground intimately in an agate pestle and mortar. The samples were then pressed as pellets and heated at  $800^\circ\text{C}$  for 12 h, then at  $1350^\circ\text{C}$  for 24 h to prepare  $\text{La}_4\text{Mg}_{3-x}(\text{Cu}, \text{Zn})_x\text{W}_3\text{O}_{18}$  where  $0 \leq x \leq 0.4$  for both solid solutions.

An issue that was faced when doping with Cu, was that  $\text{CuO}$  has a lower melting point than the reaction temperature. This meant that the samples melted in the boats. In order to combat this, a two-step thermal treatment was devised so that the Cu-doping did not melt

the sample in the alumina crucibles. This involved heating the samples first at 800°C for 6 hours and then grinding, and then heating a second time at 1300°C for 24 hours.

### 5.2.2 Double substituted $\text{La}_4\text{Mg}_3\text{W}_3\text{O}_{18}$

Stoichiometric amounts of  $\text{La}_2\text{O}_3$ ,  $\text{Fe}_2\text{O}_3$ ,  $\text{Mn}_2\text{O}_3$ ,  $\text{WO}_3$  and  $\text{Ta}_2\text{O}_5$  were ground intimately using an agate pestle and mortar. The sample was then pressed as a pellet and heated at 800°C for 12 h, then at 1350°C for 24 h to prepare  $\text{La}_4\text{Mg}_{3-x}(\text{Fe}, \text{Mn})_x\text{W}_{3-x}\text{Ta}_x\text{O}_{18}$  where  $0 \leq x \leq 0.4$  for both samples.

An issue faced with the synthesis of this solid solution, was that the melting point of  $\text{Mn}_2\text{O}_3$  was lower than the reaction temperature, meaning that, just like the Cu-doped samples, a two-step synthesis was needed to stop the samples from melting. This involved heating the samples first at 800°C for 6 hours and then grinding, and then heating a second time at 1300°C for 24 hours.

### 5.2.3 SEM/EDX analysis

SEM/EDX analysis was undertaken on a Hitachi S3400N microscope with an Oxford Instruments XMax80 EDX, with a 80mm<sup>2</sup> beam and analysed on the INCA software. Acceleration voltage was 20 kV.

Samples were characterised by PXRD, SQUID and Rietveld refinements. See Chapter 2 for more details.

## 5.3 Results and Discussion

### 5.3.1 Cu-doped $\text{La}_4\text{Mg}_3\text{W}_3\text{O}_{18}$

Room temperature PXRDs were taken for the Cu-doped solid solution (See Figure 5.1) to measure phase purity as well as unit cell size and symmetry. As can be seen from the PXRD patterns below, the samples crystallised in the lower symmetry monoclinic  $C2/m$  space group, as there was intensity at  $13^\circ 2\theta$ , which is representative of the monoclinic structure. As can be seen from the PXRD pattern (see Figure 5.1), there is an increase in the intensity of the peak at  $31^\circ 2\theta$ . Based on the PXRD patterns obtained, it was predicted that the solution limit of the Cu-doped  $\text{La}_4\text{Mg}_3\text{W}_3\text{O}_{18}$  was 0.4, meaning only a limited solid solution was attainable due to the purities of the products obtained increasing.

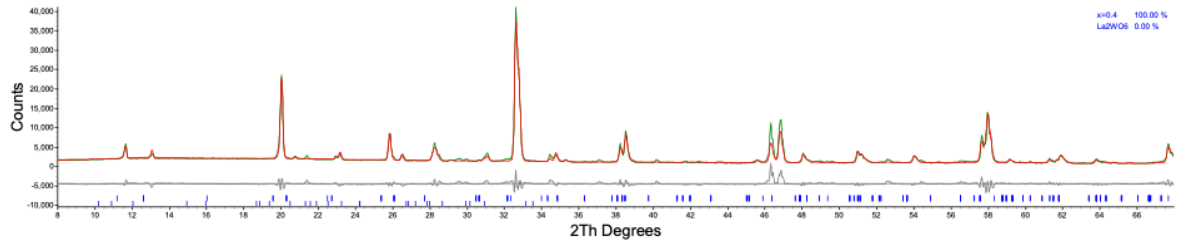


Figure 5.1: *Rietveld refinement using the PXRD pattern of  $\text{La}_4\text{Mg}_{2.6}\text{Cu}_{0.4}\text{W}_3\text{O}_{18}$ , with the red, blue and grey lines showing experimental, calculated and difference patterns respectively, fit to  $C2/m$  symmetry ( $a = 17.642628(12)$  Å,  $b = 7.822713(10)$  Å,  $c = 7.825271(12)$ ,  $\beta = 116.3404(3)^\circ$  Å,  $R_{wp} = 12.517\%$ ).*

Another thing worth noting, is the evolution of lattice parameters as the concentration of Cu increases. As can be seen from the volume plot (see figure 5.2d), there was a sharp decrease in the volume of the unit cell. This is surprising, considering the similarity in the ionic radii for  $\text{Mg}^{2+}$  and  $\text{Cu}^{2+}$  (0.72 Å and 0.73 Å, respectively). However, due to the fact that the  $\text{Cu}^{2+}$  cation has a  $d^9$  configuration, there is the possibility of the octahedra undergoing a Jahn-Teller distortion, which as can be seen from the lattice parameter plots, also affects the  $a$  parameter (see Figure 5.2a). This also means the Jahn-Teller distortions  $\text{Cu}^{2+}$  undergoes could hinder its substitution into the structure. Further experiments, such as neutron powder diffraction measurements would be needed to confirm this.

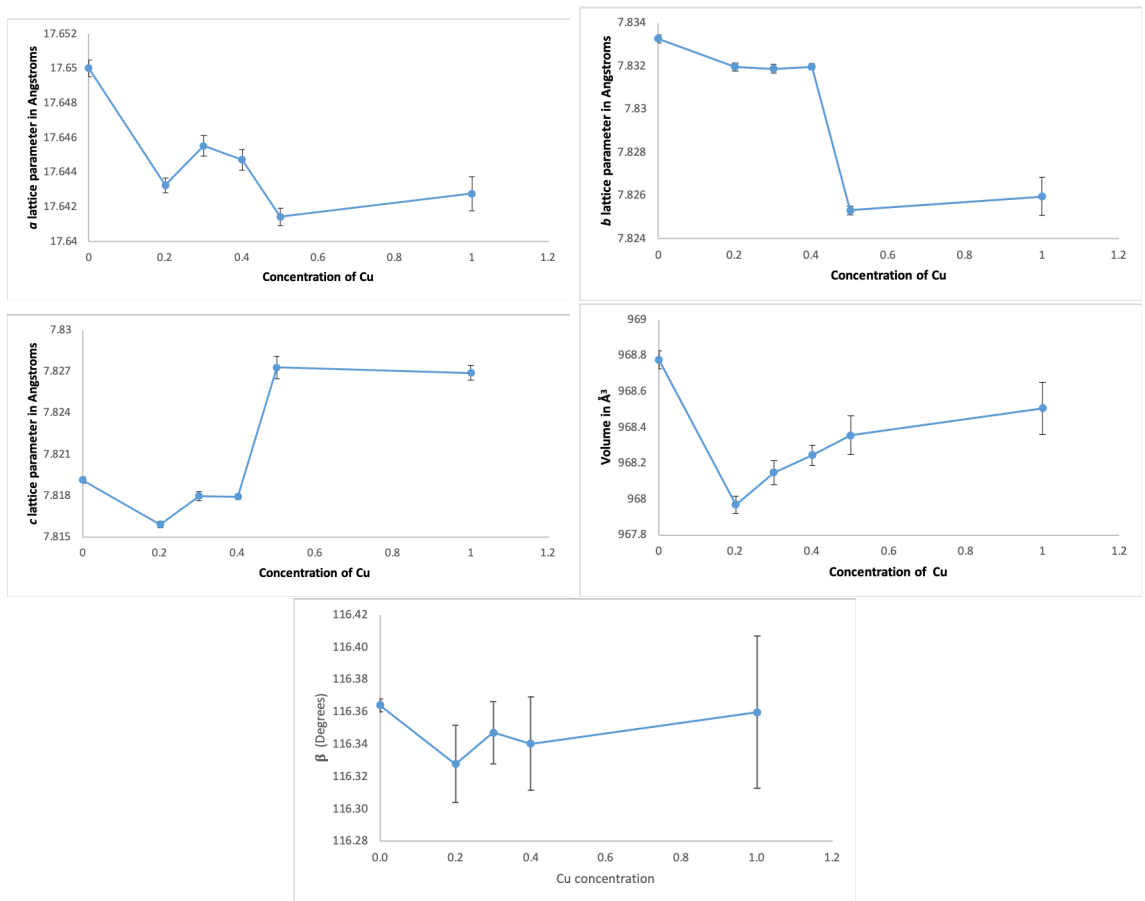


Figure 5.2: A diagram showing the lattice parameter plots for the  $\text{La}_4\text{Mg}_{3-x}\text{Cu}_x\text{W}_3\text{O}_{18}$  solid solution for the  $C2/m$  space group.

Magnetic susceptibility measurements (see Figure 5.3) were carried out on the highest concentration  $\text{La}_4\text{Mg}_{2.6}\text{Cu}_{0.4}\text{W}_3\text{O}_{18}$ . As can be seen from susceptibility, there is no evidence of long range magnetic ordering in the structure. However, the sample does not show any Curie-Weiss behaviour in the temperature range measured (see Figure 5.3). This may be due to the sample becoming more metallic on the addition of Cu (the colour of the samples in the solid solution became more black coloured as the Cu concentration increased compared to the white of the undoped sample).

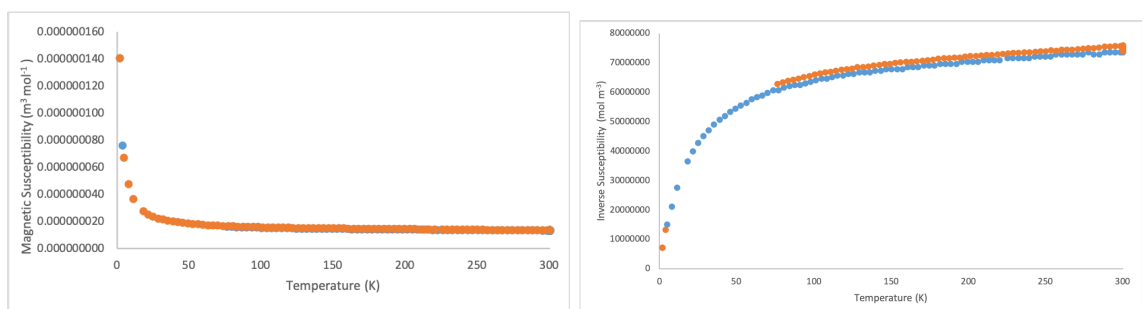


Figure 5.3: Susceptibility measurements for  $\text{La}_4\text{Mg}_{2.6}\text{Cu}_{0.4}\text{W}_3\text{O}_{18}$  (blue and orange lines correspond to ZFC and FC respectively)

### 5.3.2 Zn-doped $\text{La}_4\text{Mg}_3\text{W}_3\text{O}_{18}$

PXRD patterns were collected for this sample at room temperature to ascertain their purity, symmetry and unit cell size. PXRD patterns, there was a good fit to the  $C2/m$  model. Unlike the Cu-doped solid solution, there is not an increased peak intensity at  $31^\circ 2\theta$ . Unfortunately, the solid solution was extremely limited, only 13% doping was possible before a significant amount of impurity had appeared in the form of unreacted ZnO and  $\text{ZnWO}_6$  (see Appendix Figure 5). As can be seen from the lattice parameter plots (see Figure 5.5), there is a smooth decrease in the  $a$  parameter as well as the volume, however, the other lattice parameters do not show this smooth change. It is not clear why the solid solution is so limited given that  $\text{Mg}^{2+}$  and  $\text{Zn}^{2+}$  have similar ionic radii ( $0.72 \text{ \AA}$  and  $0.74 \text{ \AA}$  respectively).<sup>47</sup>

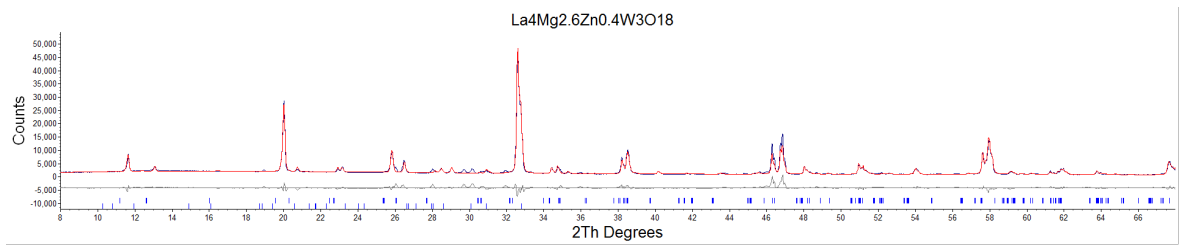


Figure 5.4: Rietveld refinement using the PXRD pattern of  $\text{La}_4\text{Mg}_{2.6}\text{Zn}_{0.4}\text{W}_3\text{O}_{18}$ , with the green, blue and grey lines showing experimental, calculated and difference patterns respectively, fit to  $Ibam$  symmetry ( $a = 17.646532(14)$   $b = 7.83328(3)$   $c = 7.819315(3)$ ,  $\beta = 116.33263^\circ(6)$   $\text{\AA}$ ,  $968.819(23) \text{ \AA}^3$ ,  $R_{wp} = 12.517\%$ ). Upper ticks correspond to the pure Zn-doped phase and the bottom ticks correspond to the  $\text{La}_2\text{WO}_6$  impurity (Le Bail fit).

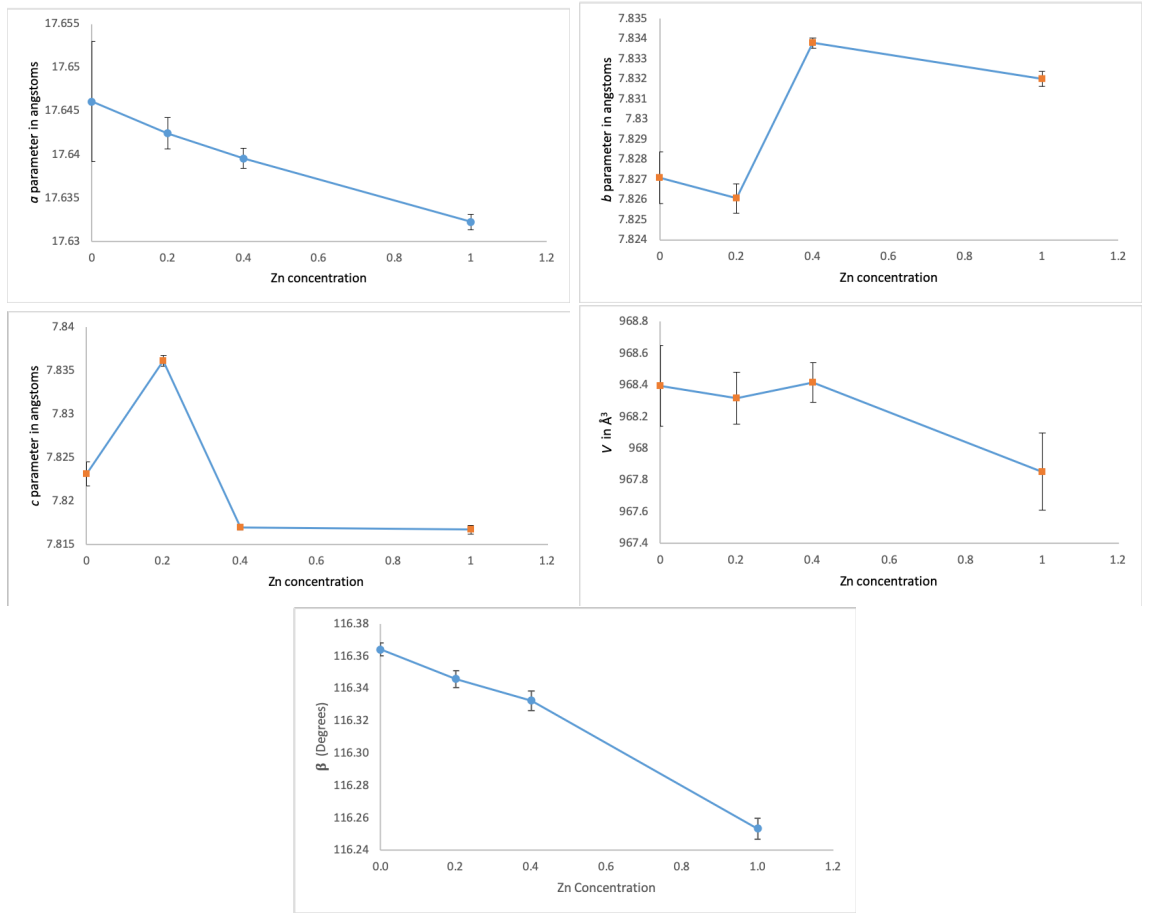


Figure 5.5: A diagram showing the Vegard's law plots for the  $\text{La}_4\text{Mg}_{3-x}\text{Zn}_x\text{W}_3\text{O}_{18}$  solid solution for the  $C2/m$  space group

### 5.3.3 Fe/Ta doped $\text{La}_4\text{Mg}_3\text{W}_3\text{O}_{18}$

Room temperature PXRD patterns were collected for the Fe/Ta doped solid solution (See Figure 5.6) to measure phase purity as well as unit cell size and symmetry. As can be seen from the PXRD patterns below, the samples crystallised in the higher symmetry  $Ibam$  space group. The main difference between the  $C2/m$  and  $Ibam$  structures is the lack of a peak at  $13^\circ 2\theta$ . As can be seen from the patterns, there is a peak that appears at approximately  $31^\circ 2\theta$ , which is attributed to the Z4 distortion. Another thing that can be seen is that there is an impurity peak at around  $35^\circ 2\theta$ , which can be attributed to the magnetic impurity  $\text{LaFeO}_3$ .

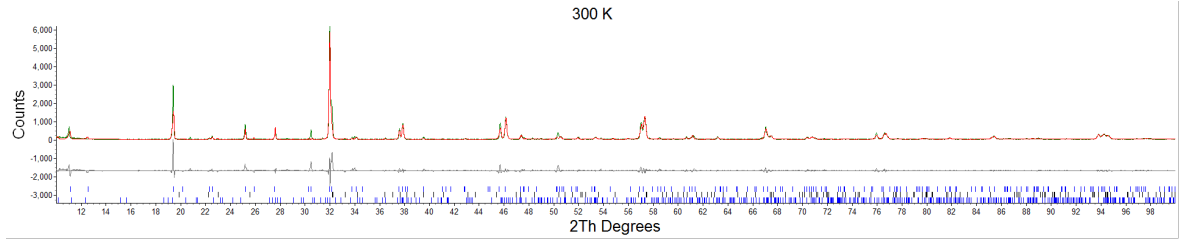


Figure 5.6: A diagram showing the PXRD pattern of  $\text{La}_4\text{Mg}_{2.4}\text{Fe}_{0.6}\text{W}_{2.4}\text{Ta}_{0.6}\text{O}_{18}$  taken at 300 K, with the green, blue and grey lines showing experimental, calculated and difference patterns respectively, fit to *Ibam* symmetry ( $a = 7.848057(3) \text{ \AA}$ ,  $b = 15.834075(4) \text{ \AA}$ ,  $c = 7.835732(7) \text{ \AA}$ ,  $R_{wp} = 24.162\%$ ). The upper ticks correspond to the pure phase, the middle ticks to the  $\text{LaFeO}_3$  impurity (92.994(3)%), middle ticks to the  $\text{LaFeO}_3$  impurity (7.006(3)%), and the bottom ticks correspond to the  $\text{La}_2\text{WO}_6$  impurity (*Le Bail fit*)

It was postulated that the phase transition in this structure (which had crystallised in the *Ibam* structure), could have a much lower phase transition temperature than the undoped sample. Variable temperature PXRD (See Figure 5.7) was done in order to ascertain whether or not the phase transition occurred at a lower temperature due to disorder on the *B*-sites. As can be seen in the PXRD pattern taken at 12 K, the structure has not made the transition from orthorhombic to monoclinic symmetry. As can be seen from the evolving lattice parameters (see Figure 5.8), there is a smooth increase in the lattice parameters, as well as the volume. This therefore suggests that there was no structural phase transition in the Fe/Ta doped sample. A possible reason for this, is that on doping of both the *B* and *B'* sites may hinder long-range octahedral rotations due to there being 4 cations occupying those sites.

SEM/EDX analysis was also done on the  $x = 0.6$  sample (see Appendix Figure 8) in order to show sample homogeneity, as well as to confirm composition of the structure. As can be seen from the SEM image, as well as the elemental maps and EDX data (see Appendix Figure 8 and 9), substitution had taken place across both *B*-sites. Again, further analysis is needed to identify the composition of the impurity phases. EDX analysis of an area indicated a ratio of La:Mg:Fe:W:Ta of 4.0(1):2.9(1):0.4(1):3.3(1):0.7(1) (see Table 2), close to the desired stoichiometry of  $\text{La}_4\text{Mg}_{2.4}\text{Fe}_{0.6}\text{W}_{2.4}\text{Ta}_{0.6}\text{O}_{18}$ , but slightly iron-deficient and tungsten rich.

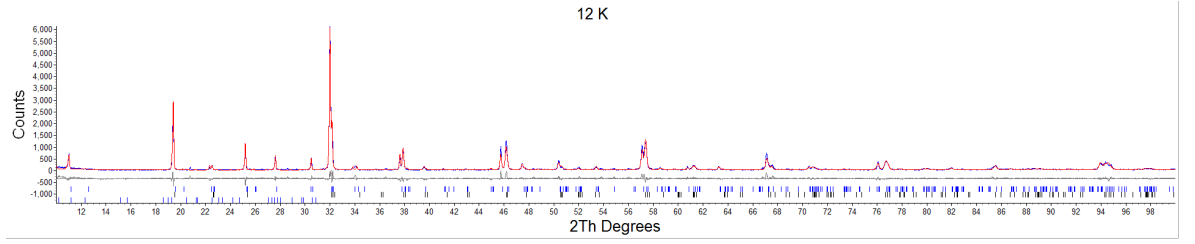


Figure 5.7: A diagram showing the PXRD pattern of  $\text{La}_4\text{Mg}_{2.4}\text{Fe}_{0.6}\text{W}_{2.4}\text{Ta}_{0.6}\text{O}_{18}$  taken at 12 K, with the pink, blue and grey lines showing experimental, calculated and difference patterns respectively, fit to *Ibam* symmetry ( $a = 7.838355(4) \text{ \AA}$ ,  $b = 15.810431(6) \text{ \AA}$ ,  $c = 7.820534(3) \text{ \AA}$ ,  $R_{wp} = 24.568\%$ ). Upper ticks correspond to the pure Fe/Ta doped phase (97.994(3)%), the middle ticks correspond to the  $\text{LaFeO}_3$  impurity (2.006(3)%) and the bottom ticks correspond to the  $\text{La}_2\text{WO}_6$  impurity (Le Bail fit).

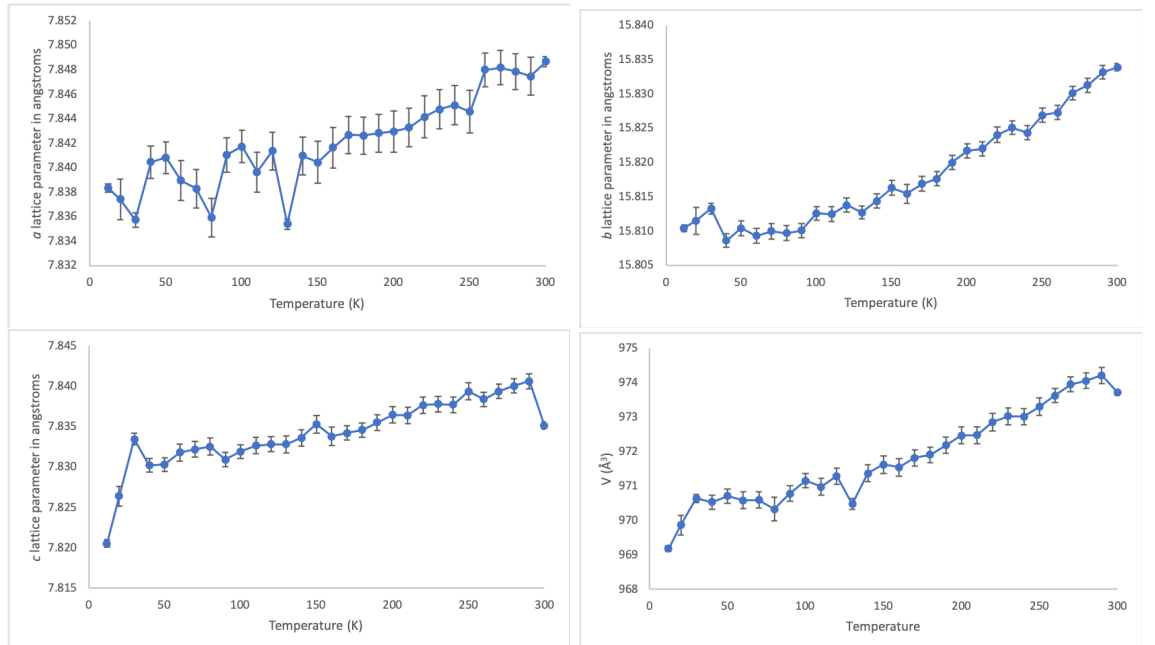


Figure 5.8: A diagram showing the evolving lattice parameters from VT-PXRD for the  $\text{La}_4\text{Mg}_{2.4}\text{Fe}_{0.6}\text{W}_{2.4}\text{Ta}_{0.6}\text{O}_{18}$  solid solution for fit to the *Ibam* space group

As can be seen from the magnetic susceptibility (see Figure 5.9), the material is paramagnetic down to 2 K. The inverse susceptibility vs T showed the sample having Curie-Weiss behaviour when  $T \geq 200$  K. A key thing to note from the T vs  $1/\chi$  data is the slight curve in the plot between 200 and 150 K. This is due to the magnetic impurity  $\text{LaFeO}_3$  (approximately 2%) being present in the sample, which made it more difficult to calculate the Weiss temperature and the effective magnetic moment per formula unit. The Weiss temperature and magnetic susceptibilities, due to the magnetic impurity were calculated using a fit above 200 K. The susceptibility calculated for  $\text{Fe}^{3+}$  ( $3d^5$ ,  ${}^6\text{I}_{7/2}$ ) was calculated to be  $5.16\mu_B$  per

$\text{Fe}^{3+}$  ion, and  $1.68 \mu_{\beta}$  per formula unit.

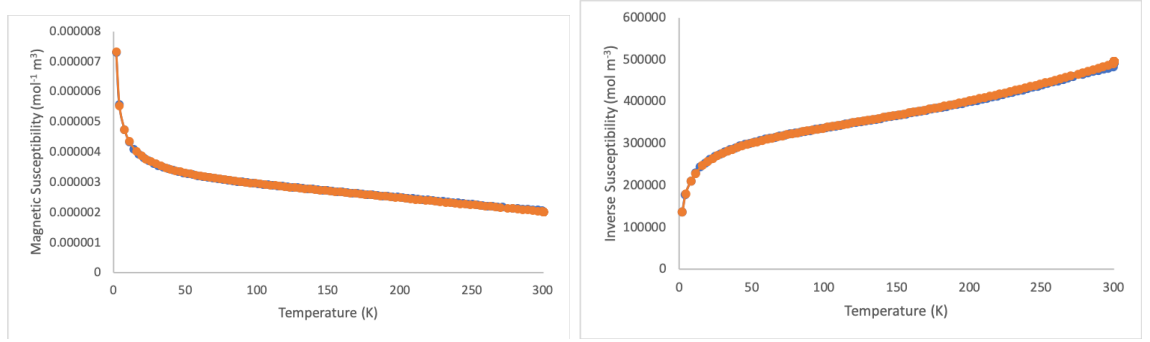


Figure 5.9:  $T$  vs  $\chi_m$  and  $T$  vs  $1/\chi_m$  plots for  $\text{La}_4\text{Mg}_{2.4}\text{Fe}_{0.6}\text{W}_{2.4}\text{Ta}_{0.6}\text{O}_{18}$  (blue line ZFC, FC line is orange)

### 5.3.4 Mn/Ta doped $\text{La}_4\text{Mg}_3\text{W}_3\text{O}_{18}$

Room temperature PXRD patterns were taken of the solid solution synthesised. As can be seen from the PXRD pattern, the  $\text{La}_4\text{Mg}_{2.8}\text{Mn}_{0.2}\text{W}_{2.8}\text{Ta}_{0.2}\text{O}_{18}$  gave a good fit to the *Ibam* model reported by Khalyavin *et al.* in 2007.<sup>36</sup> It was the purest sample obtained in the sample solution, however, the sample still contained significant impurities, thus no further analysis was done on this sample. The impurities seen in the sample below (see Figure 5.10) increased with an increase in the concentration in the dopants (see Appendix Figure 10). This suggests that the solid solution is extremely limited, which may be due to the more demanding coordination preference of the Jahn-Teller  $\text{Mn}^{3+}$  ion compared with  $\text{Mg}^{2+}$ .

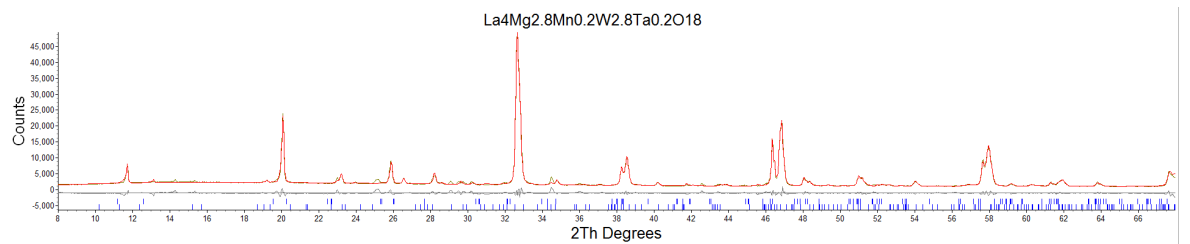


Figure 5.10: A diagram showing the PXRD pattern of  $\text{La}_4\text{Mg}_{2.8}\text{Mn}_{0.2}\text{W}_{2.8}\text{Ta}_{0.2}\text{O}_{18}$ . Upper ticks correspond to the pure Mn/Ta doped phase and the bottom ticks correspond to the  $\text{La}_2\text{WO}_6$  impurity (Le Bail fit).

## 5.4 Conclusions and Future Work

Given the similar ionic radii of  $\text{Mg}^{2+}$  and  $\text{Zn}^{2+}$  ( $0.72 \text{ \AA}$  and  $0.74 \text{ \AA}$ , respectively) ions, as well as the flexible coordination for the  $d^{10}$   $\text{Zn}^{2+}$  ion, it was thought that replacing  $\text{Mg}^{2+}$  with  $\text{Zn}^{2+}$  would have been feasible. Little change is observed in lattice parameters (which is perhaps unsurprising, due to the similar ionic radii of the cations), but the low sample purity

again suggested a very limited solid solution.

The Cu solid solution was similar, suggesting a very limited structural flexibility of the sites. The sample with the highest Cu concentration and purity ( $\text{La}_4\text{Mg}_{2.6}\text{Cu}_{0.4}\text{W}_3\text{O}_{18}$ ) was dark grey in colour (on contrast to the undoped sample), and samples only got darker with addition of more copper compared to the white colour of the undoped sample. Magnetic susceptibility measurements of this  $\text{La}_4\text{Mg}_{2.6}\text{Cu}_{0.4}\text{W}_3\text{O}_{18}$  sample suggests that doping with Cu gives a more delocalised system.

The Fe/Ta double substitution ( $\text{La}_4\text{Mg}_{3-x}\text{Fe}_x\text{W}_{3-x}\text{Ta}_x\text{O}_{18}$ ) was another attempt to introduce magnetic ions into the structure. As expected (based on the limited solid solutions for the Cu/Zn doped solid solutions), there was a very limited solid solution. The highest Fe/Ta doped sample that was investigated was  $\text{La}_4\text{Mg}_{2.4}\text{Fe}_{0.6}\text{W}_{2.4}\text{Ta}_{0.6}\text{O}_{18}$ , and even then, there was  $\text{LaFeO}_3$  impurity present, which dominated the magnetic susceptibility.

Another attempt was made to introduce magnetic ions through the double substitution of Mn/Ta. Again, the solid solution obtained was extremely limited, as can be seen from the PXRD patterns (See Appendix Figure 10). Unfortunately, the sample purity was too low to attempt any further analysis on this solid solution.

#### 5.4.1 Future Work

It would be interesting to explore whether or not the *B*-sites in this structure are more flexible than is seen in the results above. The way this could be done, is by attempting single *B*-site substitutions into the structure, using Co, Ni, and other transition metals. Something else that would be interesting to try, is to tune the octahedral tilting through doping the *A*-site with a smaller cation. Finally, it would be interesting to try some of these syntheses (such as Mn) under different conditions, so as to inhibit the possible changing of oxidation states during the reaction.

## Chapter 6

# Conclusions and future work

### 6.1 $\text{Li}^+$ insertion into the *A*-site deficient $\text{Nd}_{0.33}\text{NbO}_3$

As can be seen from the results obtained in Chapter 3, the intercalation of  $\text{Li}^+$  into the *A*-site deficient  $\text{Nd}_{0.33}\text{NbO}_3$  was successful. Characterisation by NPD shows that upon intercalation, incommensurately modulated O/Li sublattices form through out the structure, causing the broadening of superstructure peaks seen in the NPD pattern for  $\text{Nd}_{0.33}\text{NbO}_3$ . Electron diffraction analysis confirms this incommensurate modulation, as well as some diffuse scattering in the structure also, which may be due to some disorder, or short range ordering in the structure caused by these O/Li sublattices. Unfortunately, little is known about the ordering of the  $\text{Li}^+$  ions in the structure, and further analysis is required to learn about this ordering.

These results show that the tuning of *A*-site deficient perovskite structures is possible; this is significant as it may allow the tuning of more complicated structures with smaller cations, such as Li, giving these *A*-site deficient materials a wide variety of potential applications, such as battery materials, or ionic conductors.

### 6.2 *A*-site doping of the *A*-site deficient double perovskite



The results from Chapter 4 show that the parent structure,  $\text{La}_4\text{Mg}_3\text{W}_3\text{O}_{18}$  was synthesised as well as the doping of the *A*-site using Nd. They also show that, for the undoped  $\text{La}_4\text{Mg}_3\text{W}_3\text{O}_{18}$ , both crystal structures (the room temperature, low symmetry  $C2/m$ , as well as the high temperature, high symmetry *Ibam* structure) could both be isolated (the higher temperature *Ibam* structure was accessed through the quenching of  $\text{La}_4\text{Mg}_3\text{W}_3\text{O}_{18}$  at  $1100^\circ\text{C}$ ).

As can be seen from the data obtained, doping of the *A*-site worked until almost half of the

*A*-sites were equally occupied by both La and Nd. As can be seen from the lattice parameter plots, there is a smooth decrease in the volume, which suggests that the Nd was going into the structure until the occupancies were equal. However, based on the lattice parameter plots obtained (see Figure 4.6), it can be seen that there was only a limited solution, which was surprising, due to the similarity of the ionic radii of the cations. These results, although disappointing due to the possible structural inflexibility of the *A*-site, are promising, due to the potential there is to tune the *A*-site in this family of *A*-site deficient, *B*-site ordered compounds.

### 6.3 *B*-site doping of the *A*-site deficient double perovskite



Attempts to dope the *B*-site showed that the solid solutions formed were extremely limited, which suggests limited structural flexibility of the *B*-sites in this structure. In the Cu sample, this could be due to the  $\text{Cu}^{2+}$  cation being Jahn-Teller active, however further work is needed to prove this. Surprisingly, the Zn solution was also very limited; it was expected to be easier to introduce Zn to the structure, due to the flexibility of its coordination, however the sample purities say otherwise. The double *B*-site substitutions were relatively successful, however doping with Fe/Ta produced the  $\text{LaFeO}_3$  magnetic impurity after 0.6 concentration. The results shown in Chapter 5 are promising, as they show that with the right dopant (or combinations of dopants) the *B*-sites in this structure can be tuned, and properties, such as magnetic order could be induced.

### 6.4 Future work

Based on the results in Chapter 3 on  $\text{Nd}_{0.33}\text{NbO}_3$ , it would be interesting to try intercalating Na into the vacancies of the structure; the magnitude of the tilts may decrease, but there is a potential for an Na-intercalated material to become a Na-ion conductor. However, more local structural work is also required in order to learn how the cation ordering takes place upon intercalation, as well as the where the broadening of the additional peaks in the neutron powder data comes from post-intercalation. In the *A*-site double perovskites, it was shown that limited tuning could take place with the dopants tried in this thesis. However, if the right dopant was chosen, there is the potential to have a whole solid solution where the dopant occupies that site. Metals such as Co/Ni were considered, but unfortunately, due to time constraints could not be attempted. It would also be interesting to intercalate the vacancies of this structure with Li, as was done in Chapter 3, in order to see whether these structures

can be structurally tuned further.

# Bibliography

- [1] D. Beqiri, V. Cascos, J. Roberts-watts, E. R. Clark, E. Bousquet, C. Bristowe and E. E. McCabe, *Chem Comm*, 2019, **1**, 2–5.
- [2] R. G. Grebenschikov, V. F. Popova and A. K. Shirvinskaya, *Glass Phys Chem*, 2003, **29**, 194–199.
- [3] N. A. Benedek, *Inorg. Chem*, 2014, **53**, 3769–3777.
- [4] M. V. Lobanov, M. Greenblatt, E. N. Caspi, J. D. Jorgensen, D. V. Sheptyakov, B. H. Toby, C. E. Botez and P. W. Stephens, *J. Phys.: Condens. Matter*, 2004, **16**, 5339–5348.
- [5] R. H. M Paraskevopoulos, F Mayr J Hemberger, A Loidl, A. A. M. D Maurer, V Muller and A. M. Balbashov, *J. Phys.: Condens. Matter*, 2000, **12**, 3993–4011.
- [6] Z. Hu, M. Tian, B. Nysten and A. M. Jonas, *Nat Mater*, 2009, **8**, 62–67.
- [7] K. Asadi and M. A. van der Veen, *Eur J Inorg Chem*, 2016, **2016**, 4332–4344.
- [8] H. D. Megaw, *Acta Crystallogr*, 1952, **5**, 739–749.
- [9] B. Ravel, E. A. Stern, R. I. Vedrinskii and V. Kraizman, *Ferroelectrics*, 1998, **206-207**, 407–430.
- [10] N. A. Benedek, J. M. Rondinelli, H. Djani, P. Ghosez and P. Lightfoot, *Dalt Trans*, 2015, **44**, 10543–10558.
- [11] E. Bousquet, M. Dawber, N. Stucki, C. Lichtensteiger, P. Hermet, S. Gariglio, J. M. Triscone and P. Ghosez, *Nature*, 2008, **452**, 732–736.
- [12] A. I. Kingon, J.-p. Maria and S. K. Streiffer, *Nature*, 2000, **406**, 1032–1038.
- [13] M. Chen, M.-G. Ju, M. Hu, Z. Dai, Y. Hu, Y. Rong, H. Han, X. C. Zeng, Y. Zhou and N. P. Padture, *ACS Energy Lett*, 2018, **4**, 276–277.
- [14] A. D. Rae, J. G. Thompson and R. L. Withers, *Acta Crystallogr B*, 1991, **47**, 870–881.

- [15] Y. S. Hong and K. Kim, *Chem Lett*, 2000, **29**, 690–691.
- [16] B. Aurivillius and P. H. Fang, *Phys Rev*, 1962, **126**, 893–896.
- [17] S. N. Ruddlesden and P. Popper, *Acta Crystallogr*, 1958, **11**, 54–55.
- [18] B. V. Beznosikov and K. S. Aleksandrov, *Crystallogr Reports*, 2000, **45**, 792–798.
- [19] M. Dion, M. Ganne and M. Tournoux, *Mat Res Bull*, 1981, **16**, 1429–1435.
- [20] A. J. Jacobson, J. T. Lewandowski and J. W. Johnson, *Journal of The Less-Common Metals*, 1986, **116**, 137–146.
- [21] E. E. McCabe, E. Bousquet, C. P. Stockdale, C. A. Deacon, T. T. Tran, P. S. Halasyamani, M. C. Stennett and N. C. Hyatt, *Chem Mater*, 2015, **27**, 8298–8309.
- [22] Q. Z. Zhaoming Zhang, Christopher J. Howard, Brendan J. Kennedy, Kevin S. Knight, *J Solid State Chem*, 2007, **180**, 1846–1851.
- [23] Q. Zhou, P. J. Saines, N. Sharma, J. Ting, B. J. Kennedy, Z. Zhang, R. L. Withers and K. S. Wallwork, *Chem Mater*, 2008, **20**, 6666–6676.
- [24] D. Kepaptsoglou, J. D. Baran, F. Azough, D. Ekren, D. Srivastava, M. Molinari, S. C. Parker, Q. M. Ramasse and R. Freer, *Inorg.*, 2018, **57**, 45–55.
- [25] L. Carrillo, M. Villafuerte-Castrejón, G. González, L. E. Sansores, L. Bucio, J. Duque and R. Pomés, *J Mater Sci*, 2000, **35**, 3047–3052.
- [26] B. J. Kennedy, C. J. Howard, Y. Kubota and K. Kato, *J Solid State Chem*, 2004, **177**, 4552–4556.
- [27] D. A. MacLean, H. N. Ng and J. E. Greedan, *J Solid State Chem*, 1979, **30**, 35–44.
- [28] S. Roudeau, J.-M. Bassat, J.-C. Grenier, S. Pechev and F. Weill, *Comptes Rendus Chim*, 2007, **11**, 734–740.
- [29] M. Danaie, D. Kepaptsoglou, Q. M. Ramasse, C. Ophus, K. R. Whittle, S. M. Lawson, S. Pedrizzini, N. P. Young, P. A. Bagot and P. D. Edmondson, *Inorg. Chem*, 2016, **55**, 9937–9948.
- [30] A. M. Abakumov, R. Erni, A. A. Tsirlin, M. D. Rossell, D. Batuk, G. Nénert and G. V. Tendeloo, *Chem Mater*, 2013, **25**, 2670–2683.
- [31] F. Azough, D. Kepaptsoglou, Q. M. Ramasse, B. Schaffer and R. Freer, *Chem Mater*, 2015, **27**, 497–507.

- [32] C. J. Howard, B. J. Kennedy and P. M. Woodward, *Acta Crystallogr B*, 2003, **59**, 463–471.
- [33] A. K. Azad, S. A. Ivanov, S. G. Eriksson, J. Eriksen, H. Rundlöf, R. Mathieu and P. Svedlindh, *Mat Res Bull*, 2001, **36**, 2215–2228.
- [34] C. Pico, M. L. Veiga, M. A. Arillo, J. Go and L. Lo, *J Mat Chem*, 1997, **6**, 801–806.
- [35] A. M. R. S. D D Khalyavin and P. Q. Mantas, *J Phys Condens Matter*, 2005, 2585–2595.
- [36] D. D. Khalyavin, A. M. Senos, P. Q. Mantas, D. N. Argyriou, I. Tarroso Gomes, L. G. Vieira and J. L. Ribeiro, *J Solid State Chem*, 2007, **180**, 41–48.
- [37] B. J. Campbell, H. T. Stokes, D. E. Tanner and D. M. Hatch, *J Appl Cryst*, 2006, **39**, 607–614.
- [38] H. M. Rietveld, *J Appl Cryst*, 1969, **2**, 65–71.
- [39] A. A. Coelho, *J Appl Cryst*, 2003, **36**, 86–95.
- [40] R. A. Young, *TheRietveldMethod.pdf*, J. Appl. Cryst., 2nd edn., 1993.
- [41] G. Kresse and J. Hafner, *Phys Rev B*, 1993, **47**, 558.
- [42] G. Kresse and J. Furthmüller, *Comp Mat Sci*, 2007, **99**, 16–29.
- [43] X. Gonze, F. Jollet, F. Abreu Araujo, D. Adams, B. Amadon, T. Applencourt, C. Audouze, J. M. Beuken, J. Bieder, A. Bokhanchuk, E. Bousquet, F. Bruneval, D. Caliste, M. Côté, F. Dahm, F. Da Pieve, M. Delaveau, M. Di Gennaro, B. Dorado, C. Espejo, G. Geneste, L. Genovese, A. Gerossier, M. Giantomassi, Y. Gillet, D. R. Hamann, L. He, G. Jomard, J. Laflamme Janssen, S. Le Roux, A. Levitt, A. Lherbier, F. Liu, I. Lukačević, A. Martin, C. Martins, M. J. Oliveira, S. Poncé, Y. Pouillon, T. Rangel, G. M. Rignanese, A. H. Romero, B. Rousseau, O. Rubel, A. A. Shukri, M. Stankovski, M. Torrent, M. J. Van Setten, B. Van Troeye, M. J. Verstraete, D. Waroquiers, J. Wiktor, B. Xu, A. Zhou and J. W. Zwanziger, *Comp Phys Comm*, 2016, **205**, 106–131.
- [44] J. P. Perdew, A. Ruzsinszky, G. I. Csonka, O. A. Vydrov, G. E. Scuseria, L. A. Constantin, X. Zhou and K. Burke, *Phys Rev Lett*, 2007, **136406**, 1–4.
- [45] A. Nadiri, G. Le Flem and C. Delmas, *J Solid State Chem*, 1988, **73**, 338–347.
- [46] A. Yamamoto, H. Uchiyama and S. Tajima, *Mat Res Bull*, 2004, **39**, 1691–1699.
- [47] R. D. Shannon, *Acta Crystallogr*, 1976, **A32**, 751.
- [48] A. R. West, *Solid State Chemistry and its Applications*, John Wiley & Sons, 1984.

# Appendix

## Nd-doped $\text{La}_4\text{Mg}_3\text{W}_3\text{O}_{18}$

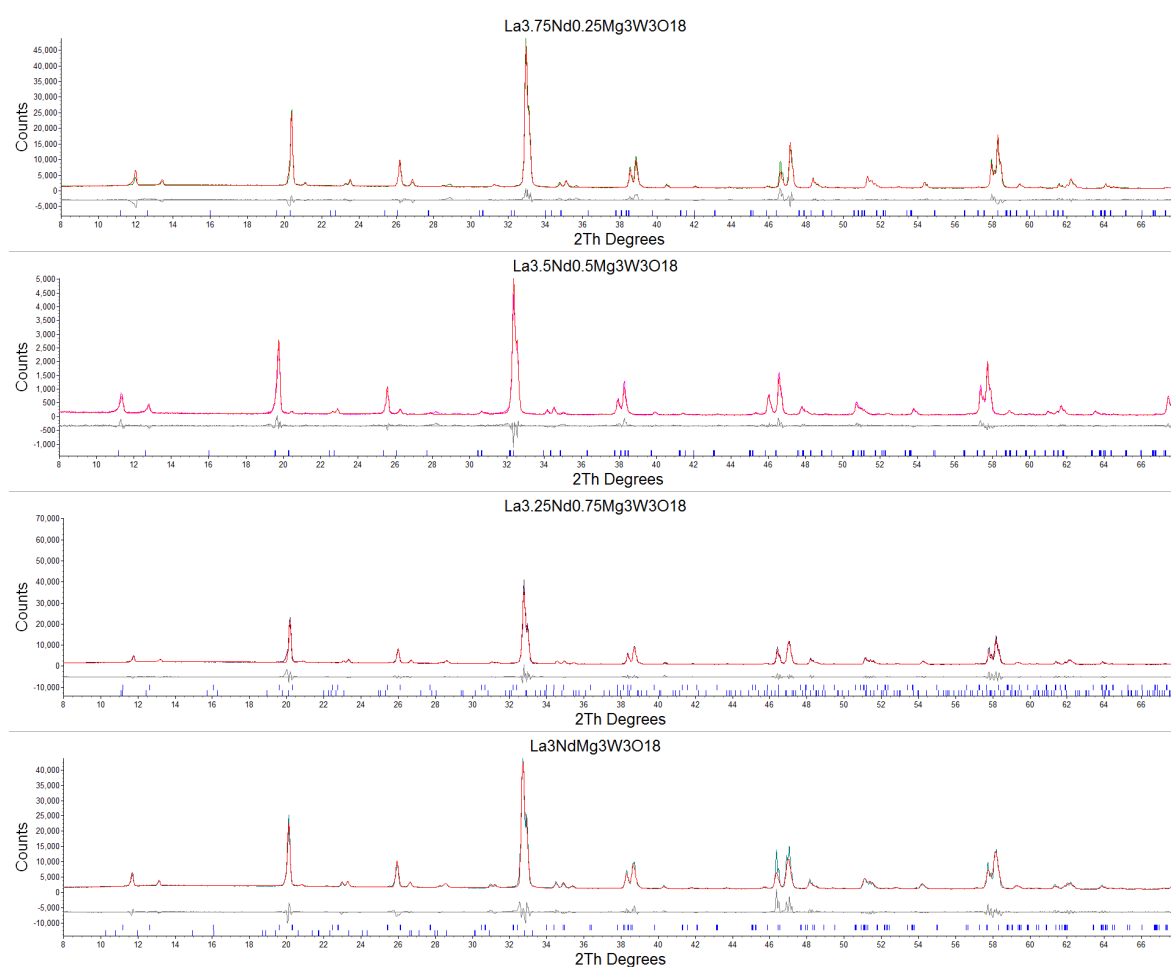


Figure 1: Various figures showing Rietveld refinement profiles from PXRD patterns obtained from the Nd-doped  $\text{La}_4\text{Mg}_3\text{W}_3\text{O}_{18}$  solid solution. Upper ticks are shown for the pure doped samples and the lower ticks are for the  $\text{La}_2\text{WO}_6$  impurity (LeBail fit)

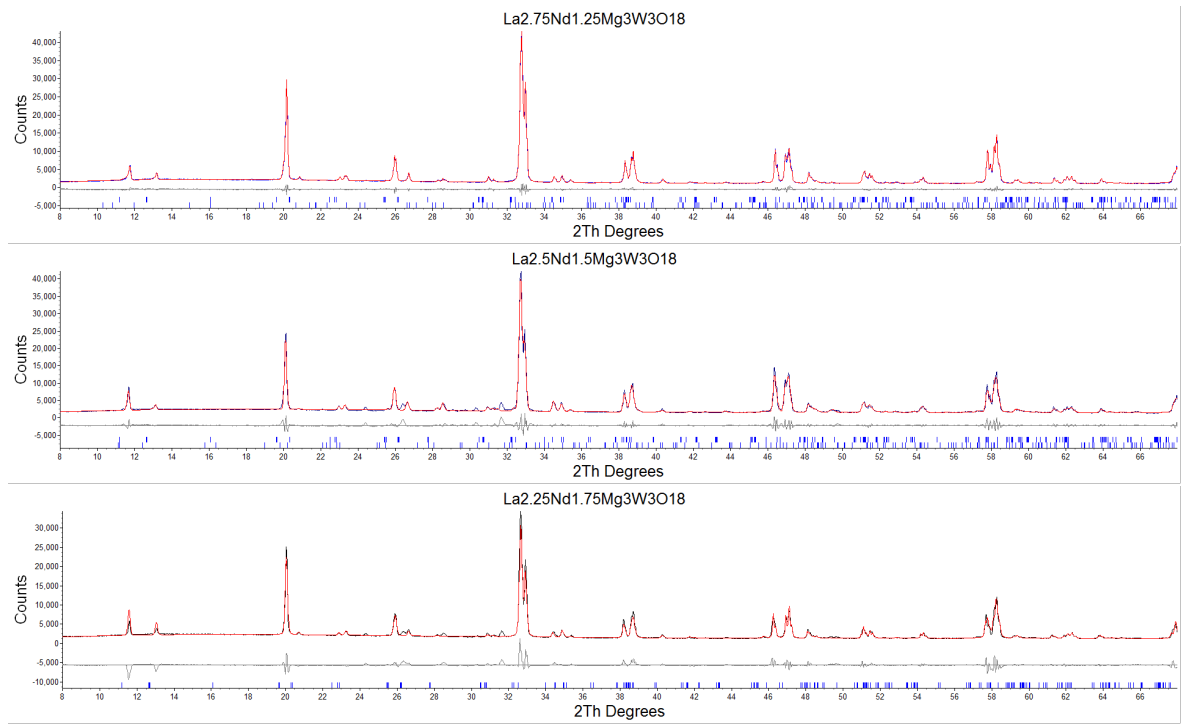


Figure 1: *Continued from page 56*

Table 1: *A table showing the evolution in lattice parameters with varying Nd concentrations*

Nd Concentration	$a$ (Å)	$b$ (Å)	$c$ (Å)	$V$ (Å <sup>3</sup> )	$\beta$ (Degrees)
0	17.646093 (7)	7.8271 (2)	7.823169 (4)	968.397 (2)	116.36421 (4)
0.25	17.641052 (3)	7.821174 (6)	7.821006 (7)	967.148 (7)	116.32932 (2)
0.5	17.637554 (2)	7.81576 (3)	7.814828 (7)	965.731 (3)	116.279 (2)
0.75	17.638779 (2)	7.810049 (3)	7.817758 (4)	964.58 (4)	116.2936 (1)
1	17.6418 (3)	7.7966508 (5)	7.80995 (5)	963.688 (8)	116.31271 (1)
1.25	17.635637(4)	7.786104 (9)	7.816696 (1)	962.529 (9)	116.31825 (1)
1.5	17.632654 (3)	7.7806 (8)	7.810029 (8)	960.484 (3)	116.31644 (6)
1.75	17.635625 (8)	7.783181 (4)	7.806352 (9)	956.297 (6)	116.3234 (8)
2	17.63347 (3)	7.787392 (8)	7.808331 (8)	962.696 (4)	116.33256 (4)
2.25	17.635737 (2)	7.788748 (1)	7.754346 (1)	956.071 (9)	116.33455 (4)

SEM + EDX data for  $\text{La}_2\text{Nd}_2\text{Mg}_3\text{W}_3\text{O}_{18}$

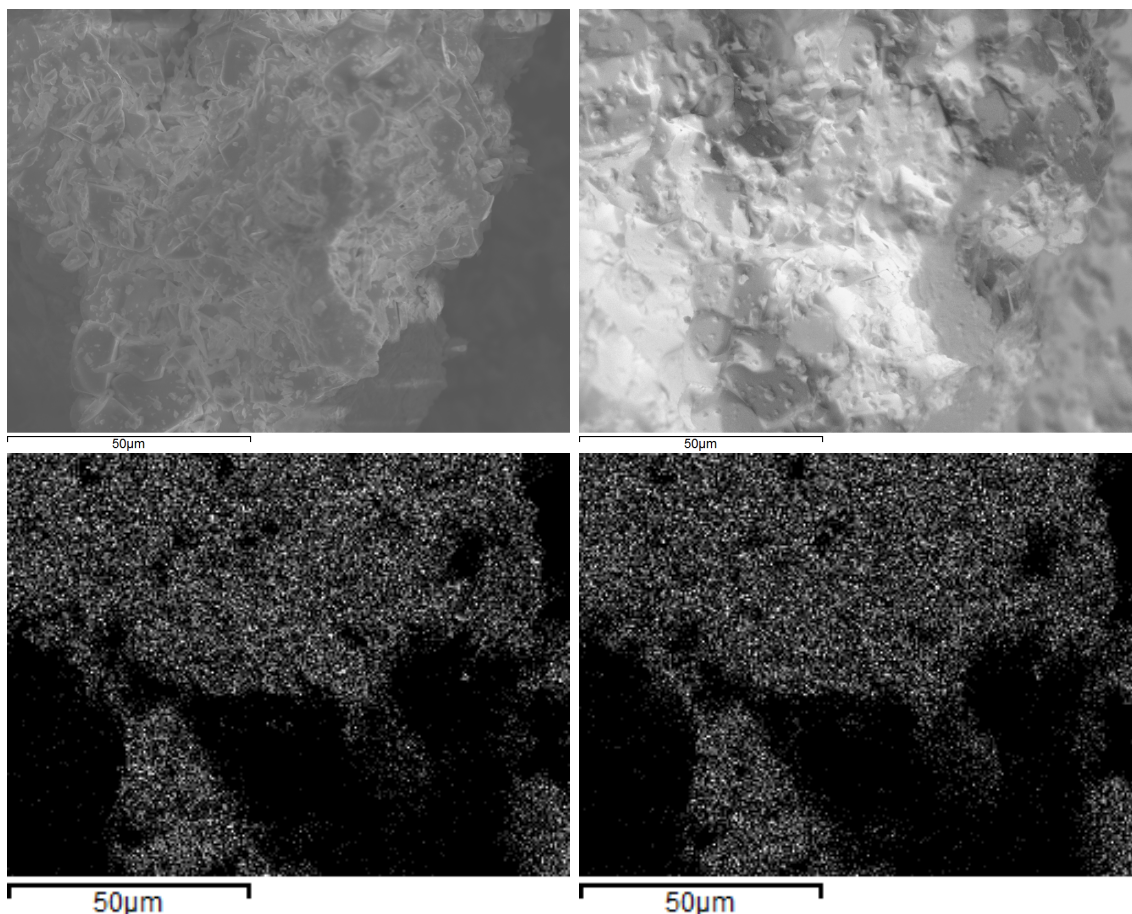


Figure 2: Various figures showing SEM images and the element maps for  $\text{La}_2\text{Nd}_2\text{Mg}_3\text{W}_3\text{O}_{18}$ . Images (from top left to right), secondary electron image for  $\text{La}_2\text{Nd}_2\text{Mg}_3\text{W}_3\text{O}_{18}$ , backscattering electron image for  $\text{La}_2\text{Nd}_2\text{Mg}_3\text{W}_3\text{O}_{18}$ , Nd element map, La element map

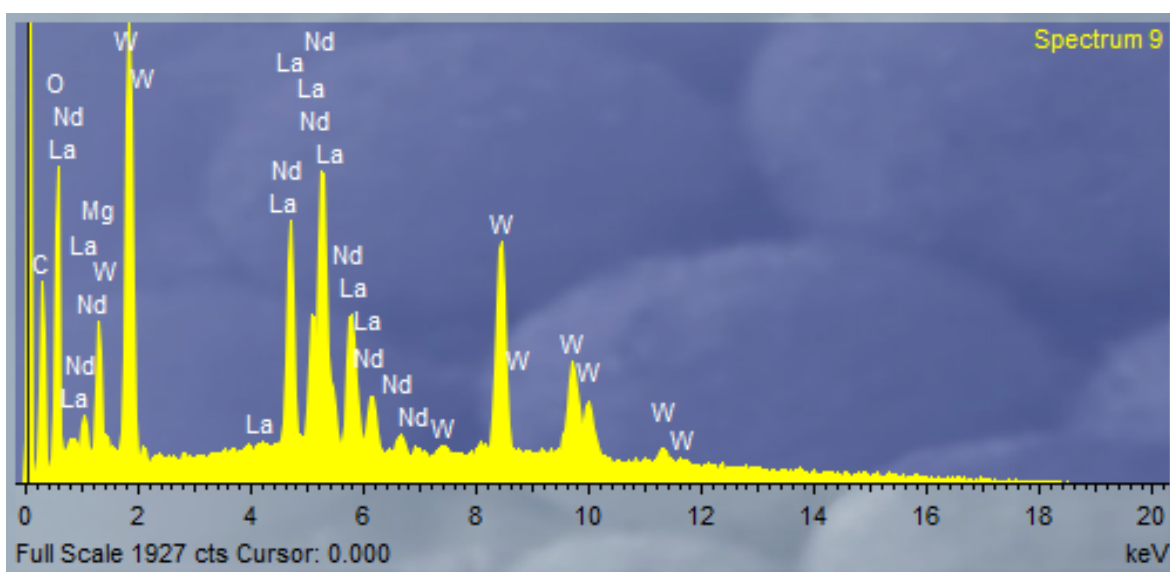


Figure 3: figure showing the EDX pattern for  $\text{La}_2\text{Nd}_2\text{Mg}_3\text{W}_3\text{O}_{18}$

Table 2: *A table showing the atomic weight percentages of elements in  $La_2Nd_2Mg_3W_3O_{18}$  based on EDX*

Element	Atomic%
Mg	30.02
La	18.96
Nd	19.03
W	31.99

# Cu-doped $\text{La}_4\text{Mg}_3\text{W}_3\text{O}_{18}$

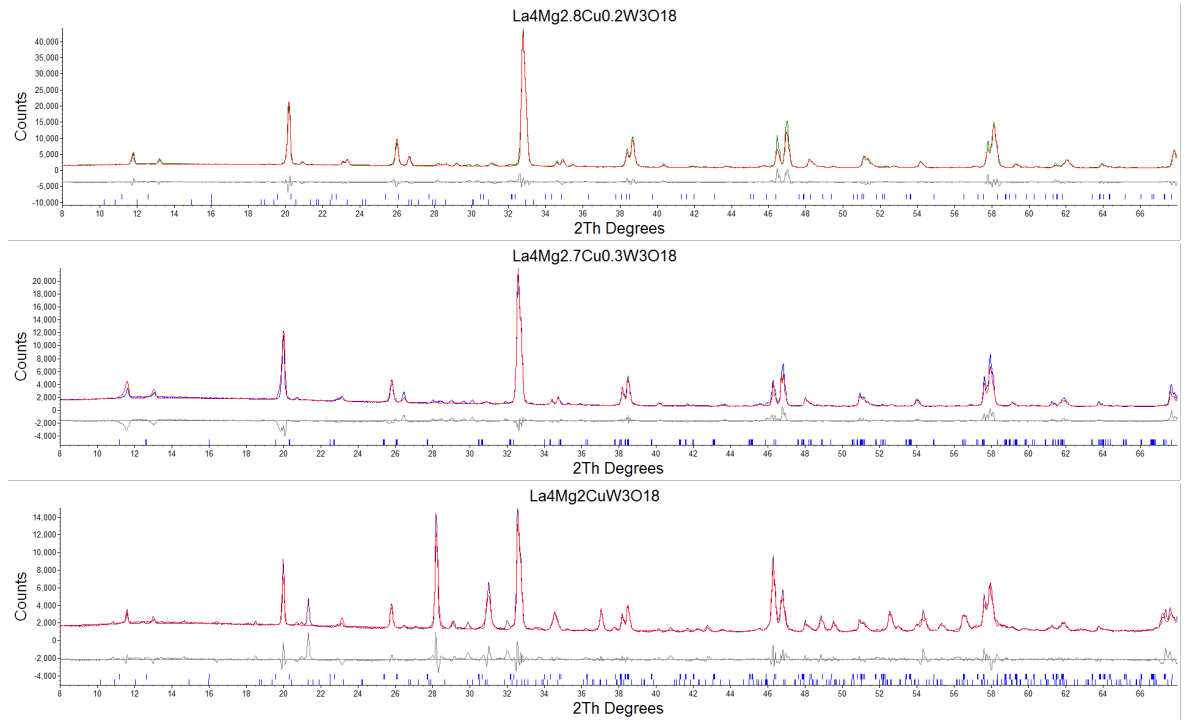


Figure 4: Various figures showing Rietveld refinement profiles from PXRD patterns obtained from the Cu-doped  $\text{La}_4\text{Mg}_3\text{W}_3\text{O}_{18}$  solid solution. Upper ticks show the pure Cu-doped sample, lower ticks show the  $\text{La}_2\text{WO}_6$  impurity (LeBail fit).

Table 3: A table showing the evolving lattice parameters in Cu-doped  $\text{La}_4\text{Mg}_3\text{W}_3\text{O}_{18}$  with increasing concentrations of Cu

Cu Concentration	$a$ (Å)	$b$ (Å)	$c$ (Å)	$V$ (Å <sup>3</sup> )	$\beta$ (Degrees)
0	17.646075 (6)	7.827105 (1)	7.823139 (4)	968.394	116.36421 (4)
0.2	17.642633 (3)	7.82429 (1)	7.82435 (1)	968.141	116.32788 (2)
0.3	17.641381 (3)	7.824045 (1)	7.821402 (2)	967.413	116.34716 (1)
0.4	17.642628 (2)	7.82271 (1)	7.825271 (2)	967.808	116.34038 (2)
1	17.640022 (6)	7.814872 (6)	7.825789 (5)	966.812	116.35984 (4)

# Zn-doped $\text{La}_4\text{Mg}_3\text{W}_3\text{O}_{18}$

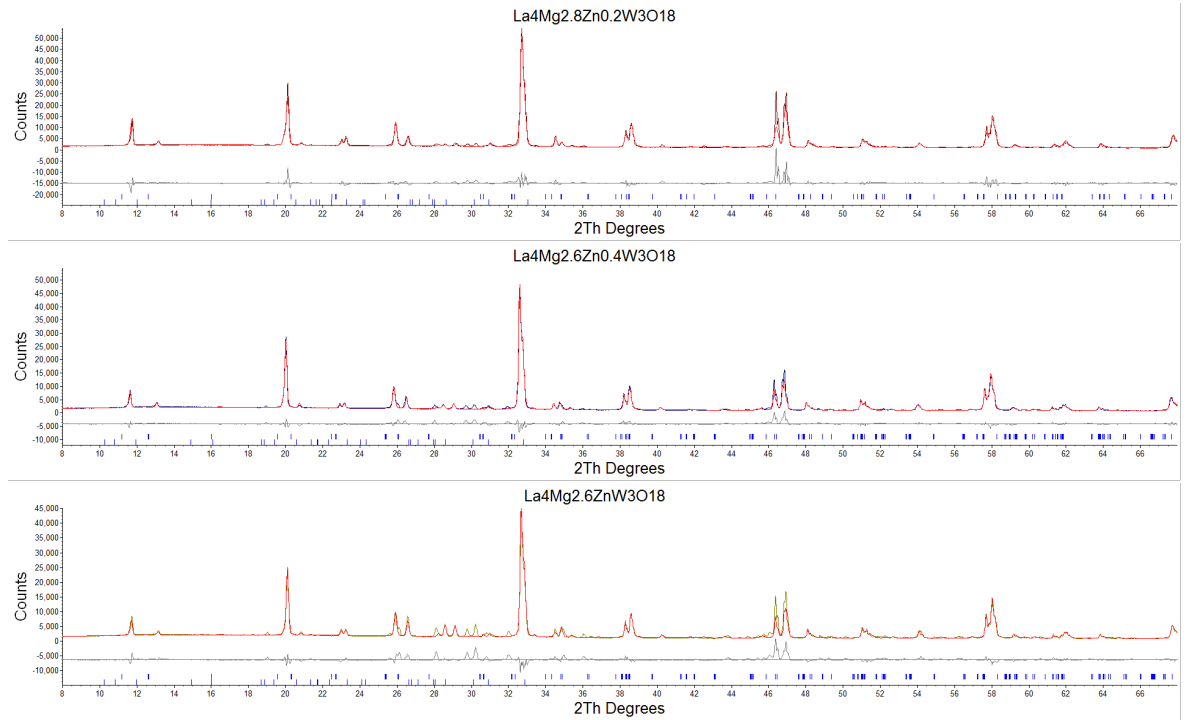


Figure 5: Various figures showing Rietveld refinement profiles from PXRD patterns obtained from the Zn-doped  $\text{La}_4\text{Mg}_3\text{W}_3\text{O}_{18}$  solid solution. Upper ticks show the pure Cu-doped sample, lower ticks show the  $\text{La}_2\text{WO}_6$  impurity (LeBail fit).

Table 4: A table showing the varying lattice parameters with varying Zn concentrations

Zn Concentration	$a$ (Å)	$b$ (Å)	$c$ (Å)	$V$ (Å <sup>3</sup> )	$\beta$ (Degrees)
0	17.646075 (6)	7.827105 (2)	7.823139 (4)	968.394 (14)	116.36421 (4)
0.2	17.644115 (2)	7.82694 (8)	7.824378 (9)	968.308 (8)	116.34587 (5)
0.4	17.646532 (4)	7.833282 (3)	7.819315 (3)	968.819 (23)	116.33263 (6)
1	17.634484 (2)	7.830509 (4)	7.816503 (4)	968.017 (16)	116.25345 (6)

# Fe/Ta-doped $\text{La}_4\text{Mg}_3\text{W}_3\text{O}_{18}$

## RT PXRD patterns

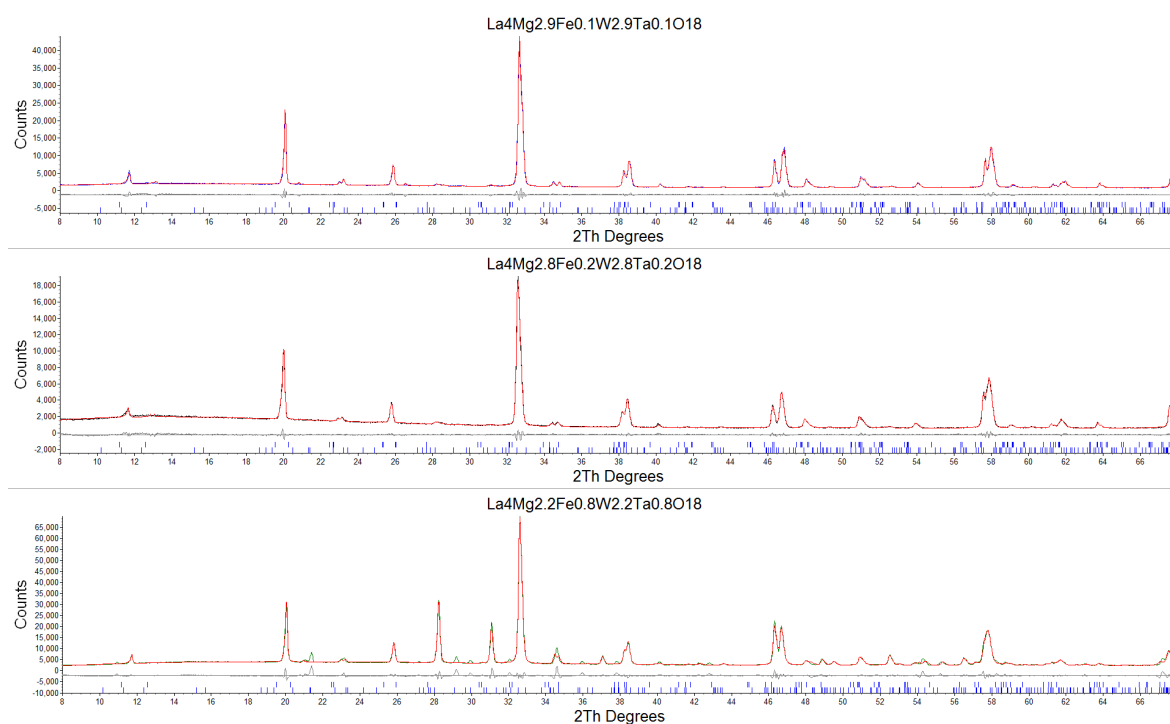


Figure 6: Various figures showing Rietveld refinement profiles from PXRD patterns obtained from the Fe/Ta-doped  $\text{La}_4\text{Mg}_{3-x}\text{Fe}_x\text{W}_{3-x}\text{Ta}_x\text{O}_{18}$ . Upper ticks show the pure Cu-doped sample, lower ticks show the  $\text{La}_2\text{WO}_6$  impurity (LeBail fit).

# VT PXR D patterns for $\text{La}_4\text{Mg}_{2.4}\text{Fe}_{0.6}\text{W}_{2.4}\text{Ta}_{0.6}\text{O}_{18}$

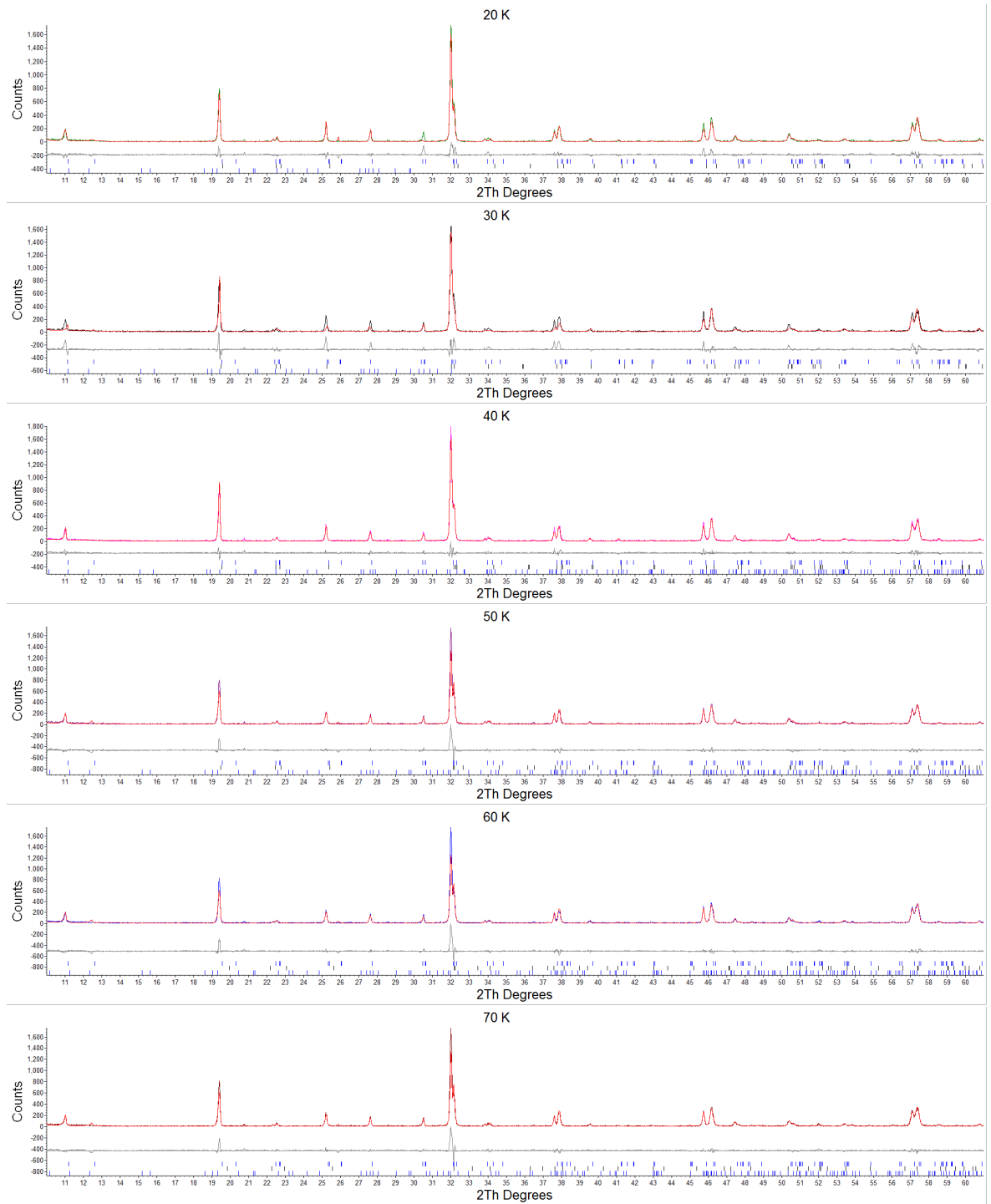


Figure 7: Various figures showing the Variable Temperature PXR D patterns for the  $\text{Cu}$ -doped  $\text{La}_4\text{Mg}_{2.4}\text{Fe}_{0.6}\text{W}_{2.4}\text{Ta}_{0.6}\text{O}_{18}$  in the 12 K to 300 K temperature range. Upper ticks correspond to the pure  $\text{Fe}/\text{Ta}$  doped phase (97.994(3)%), middle ticks to the  $\text{LaFeO}_3$  impurity (2.006(3)%), and the bottom ticks correspond to the  $\text{La}_2\text{WO}_6$  impurity (LeBail fit)

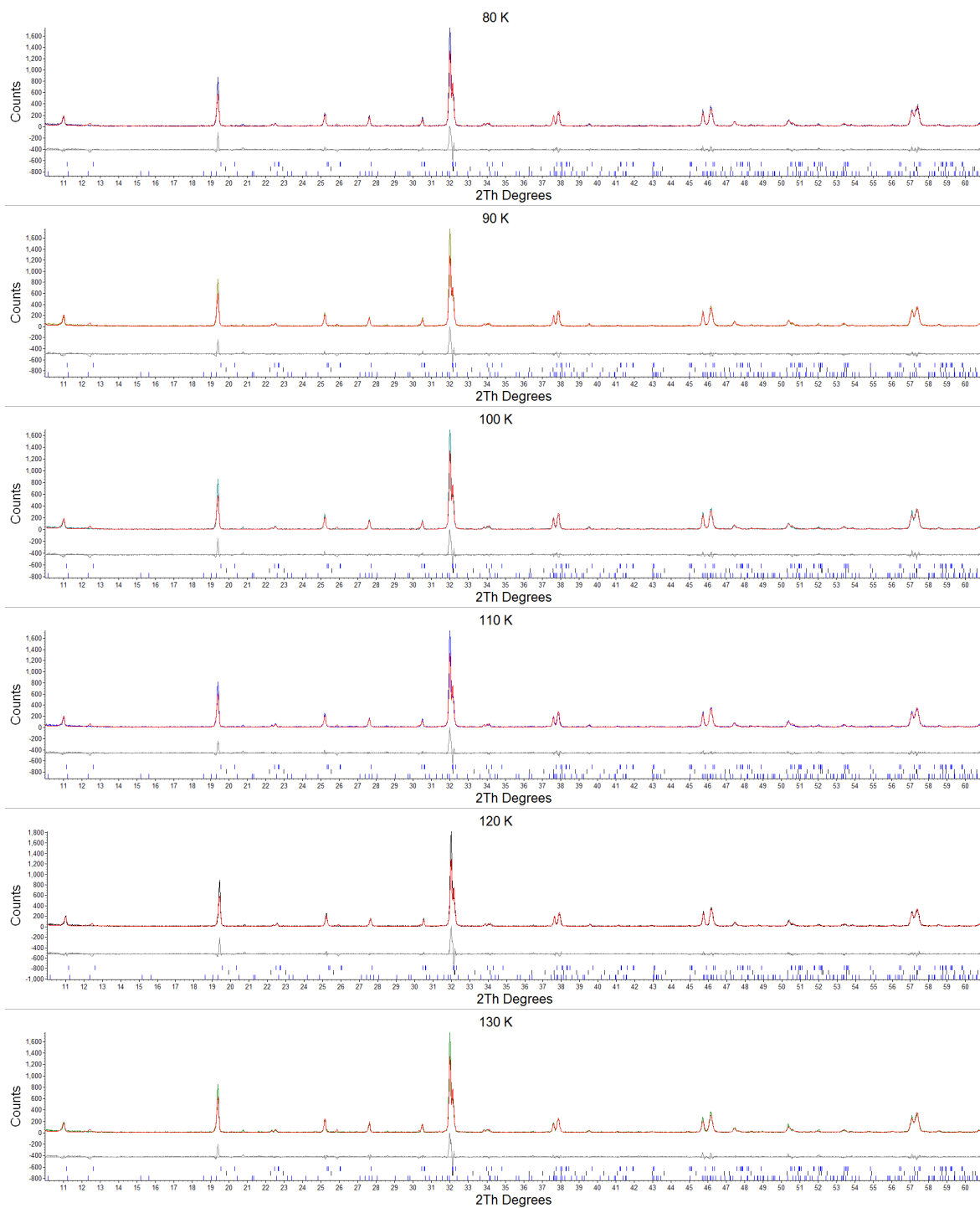


Figure 7: *Continued from page 63*

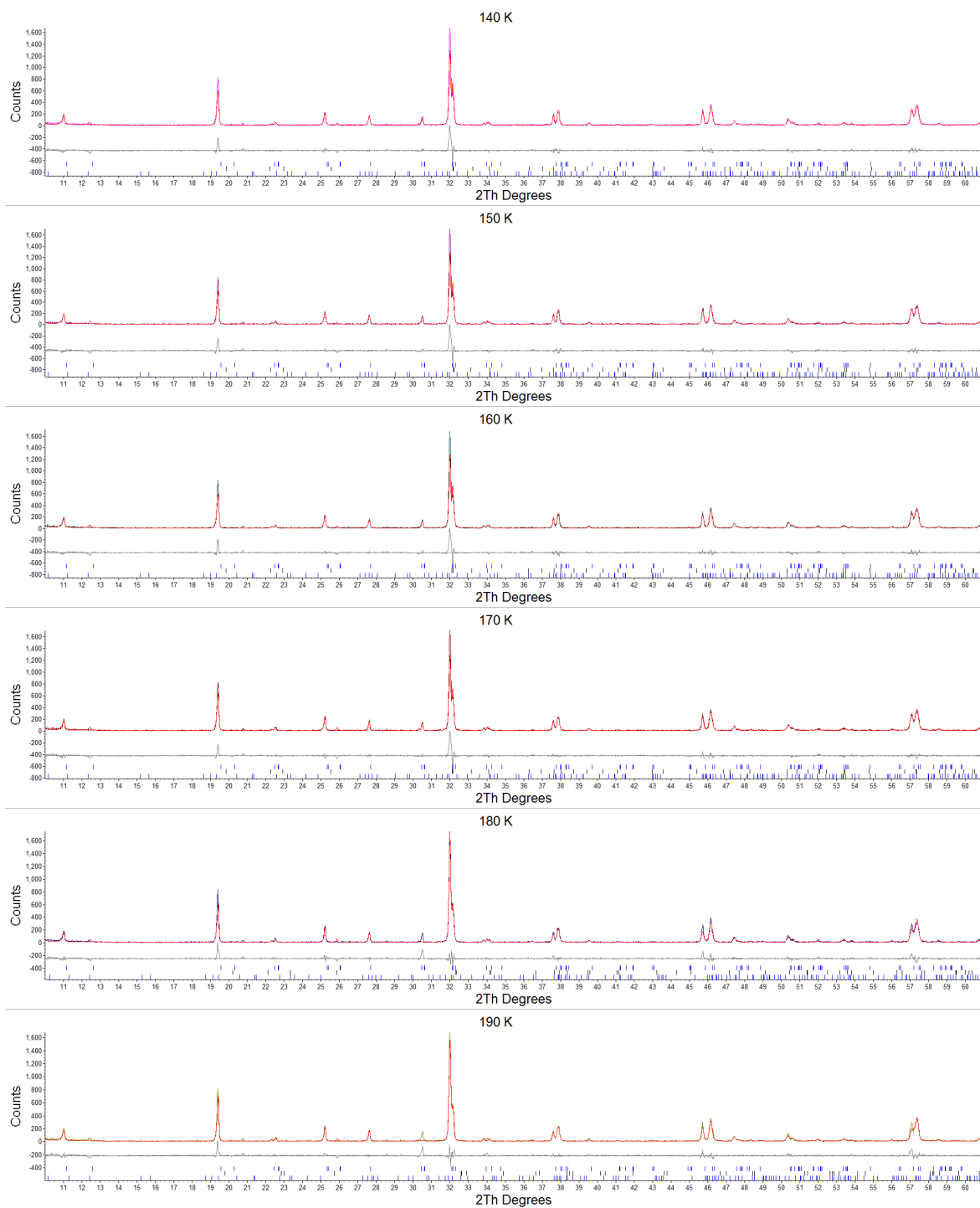


Figure 7: *Continued from page 63*

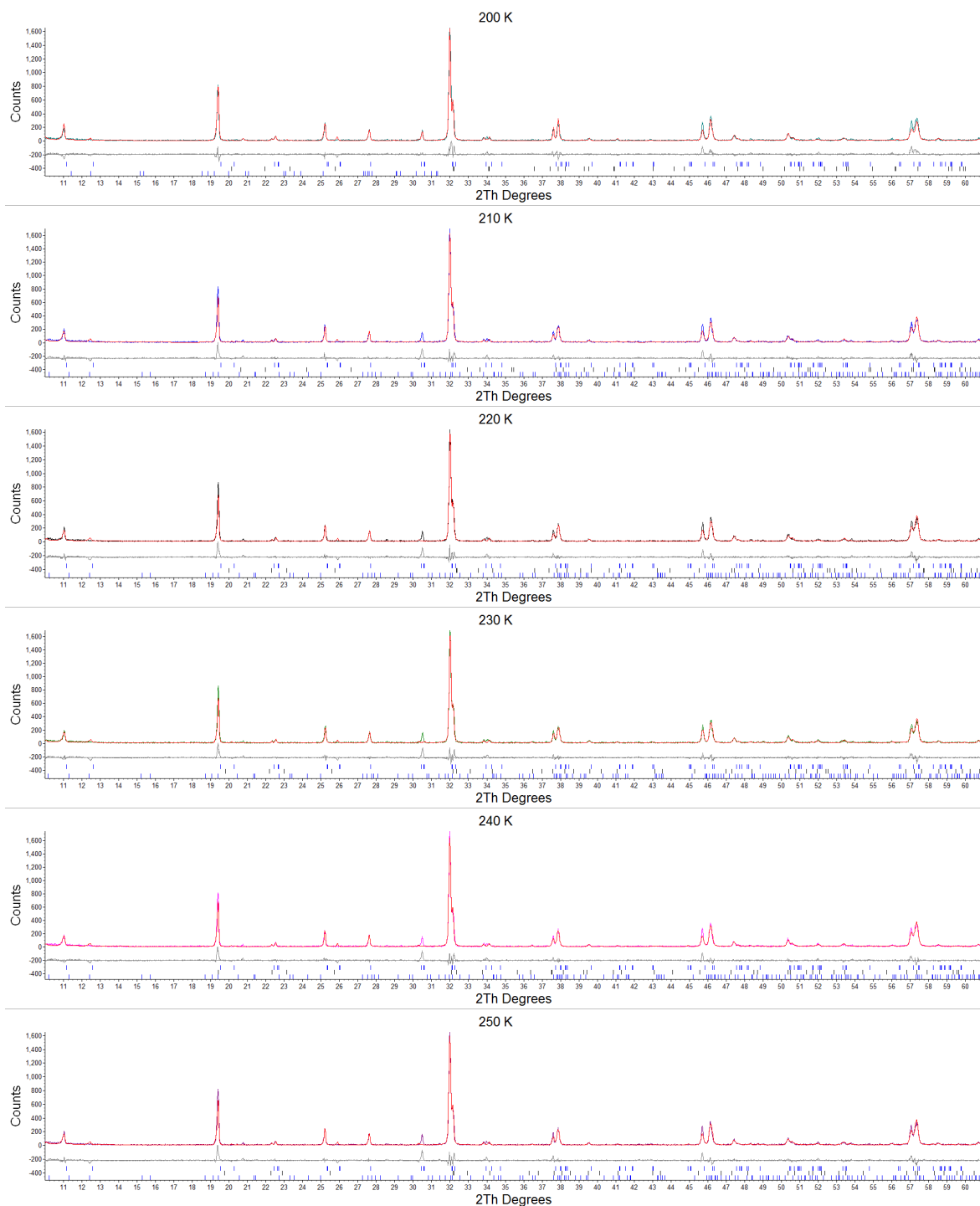


Figure 7: *Continued from page 63*

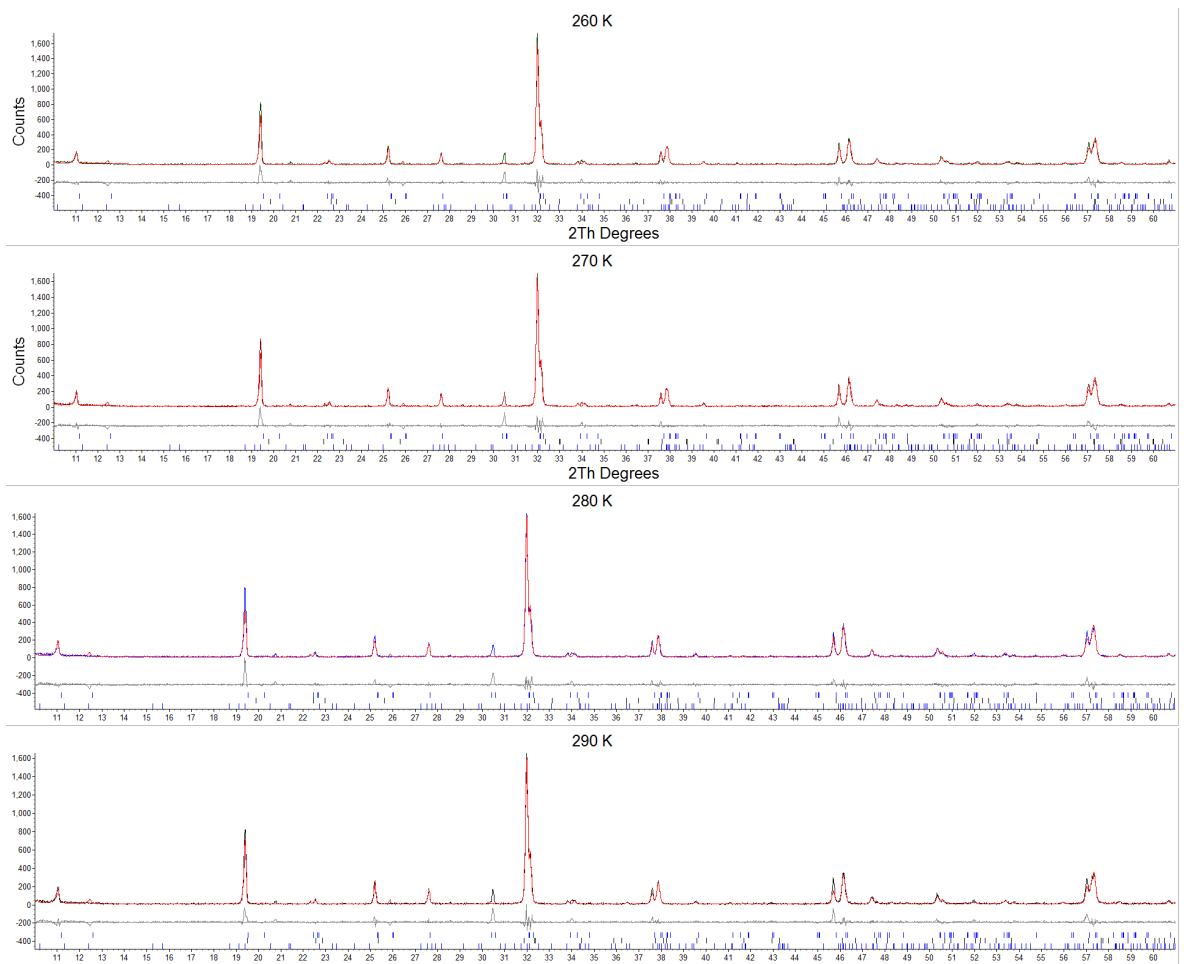


Figure 7: *Continued from page 63*

## SEM and EDX data for $\text{La}_4\text{Mg}_{2.4}\text{Fe}_{0.6}\text{W}_{2.4}\text{Ta}_{0.6}\text{O}_{18}$

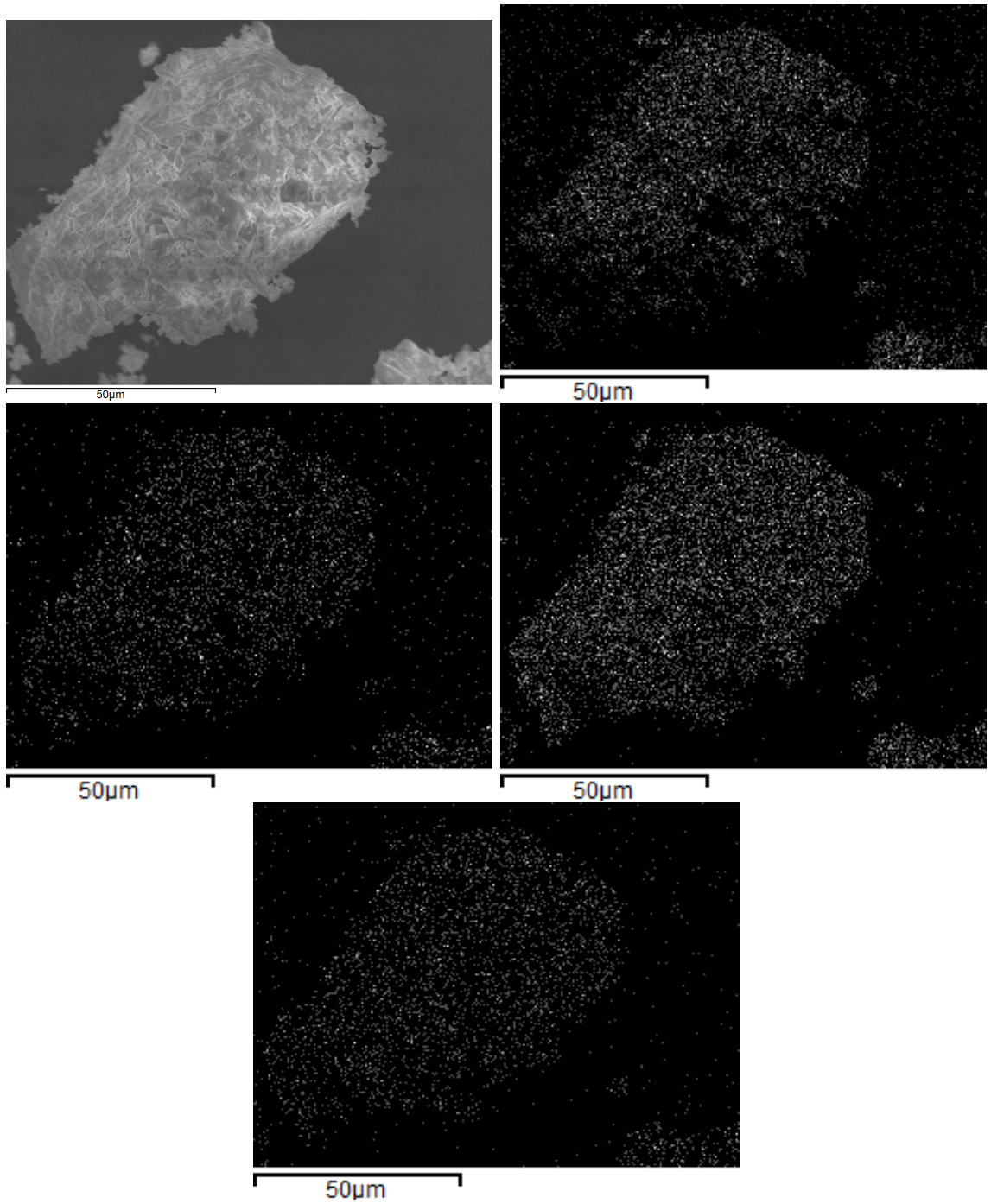


Figure 8: Various figures showing SEM images and the element maps for  $\text{La}_4\text{Mg}_{2.4}\text{Fe}_{0.6}\text{W}_{2.4}\text{Ta}_{0.6}\text{O}_{18}$ . Images (from top left to right), secondary electron image for  $\text{La}_4\text{Mg}_{2.4}\text{Fe}_{0.6}\text{W}_{2.4}\text{Ta}_{0.6}\text{O}_{18}$ , Mg element map, Fe element map, W element map, Ta element map

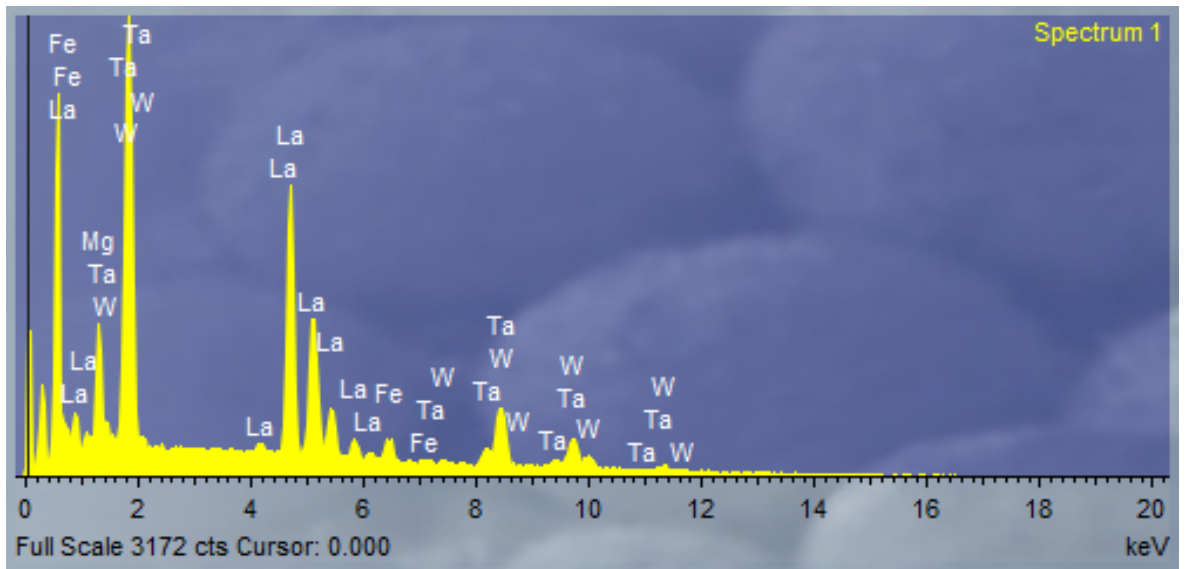


Figure 9: figure showing the EDX pattern for  $La_4Mg_{2.4}Fe_{0.6}W_{2.4}Ta_{0.6}O_{18}$

Table 5: A table showing the atomic weight percentages of elements in  $La_4Mg_{2.4}Fe_{0.6}W_{2.4}Ta_{0.6}O_{18}$  based on EDX

Element	Atomic%
Mg	25.24
Fe	4.11
La	35.34
Ta	5.82
W	29.49

# Mn/Ta-doped $\text{La}_4\text{Mg}_3\text{W}_3\text{O}_{18}$

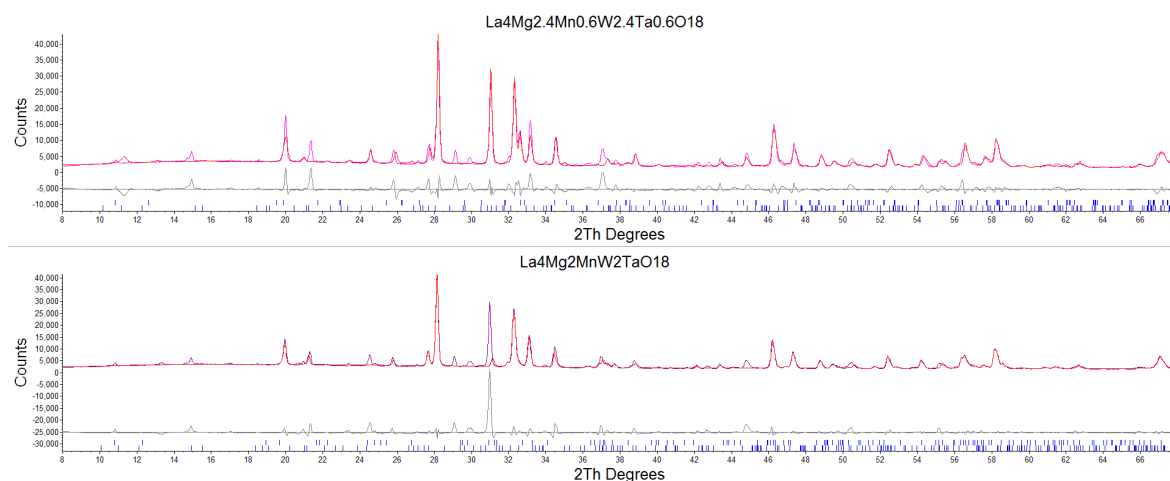


Figure 10: Various figures showing the PXR D patterns for the Mn/Ta-doped  $\text{La}_4\text{Mg}_{3-x}\text{Mn}_x\text{W}_{3-x}\text{Ta}_x\text{O}_{18}$ . Upper ticks correspond to the pure Mn/Ta doped phase and the bottom ticks correspond to the  $\text{La}_2\text{WO}_6$  impurity (LeBail fit)